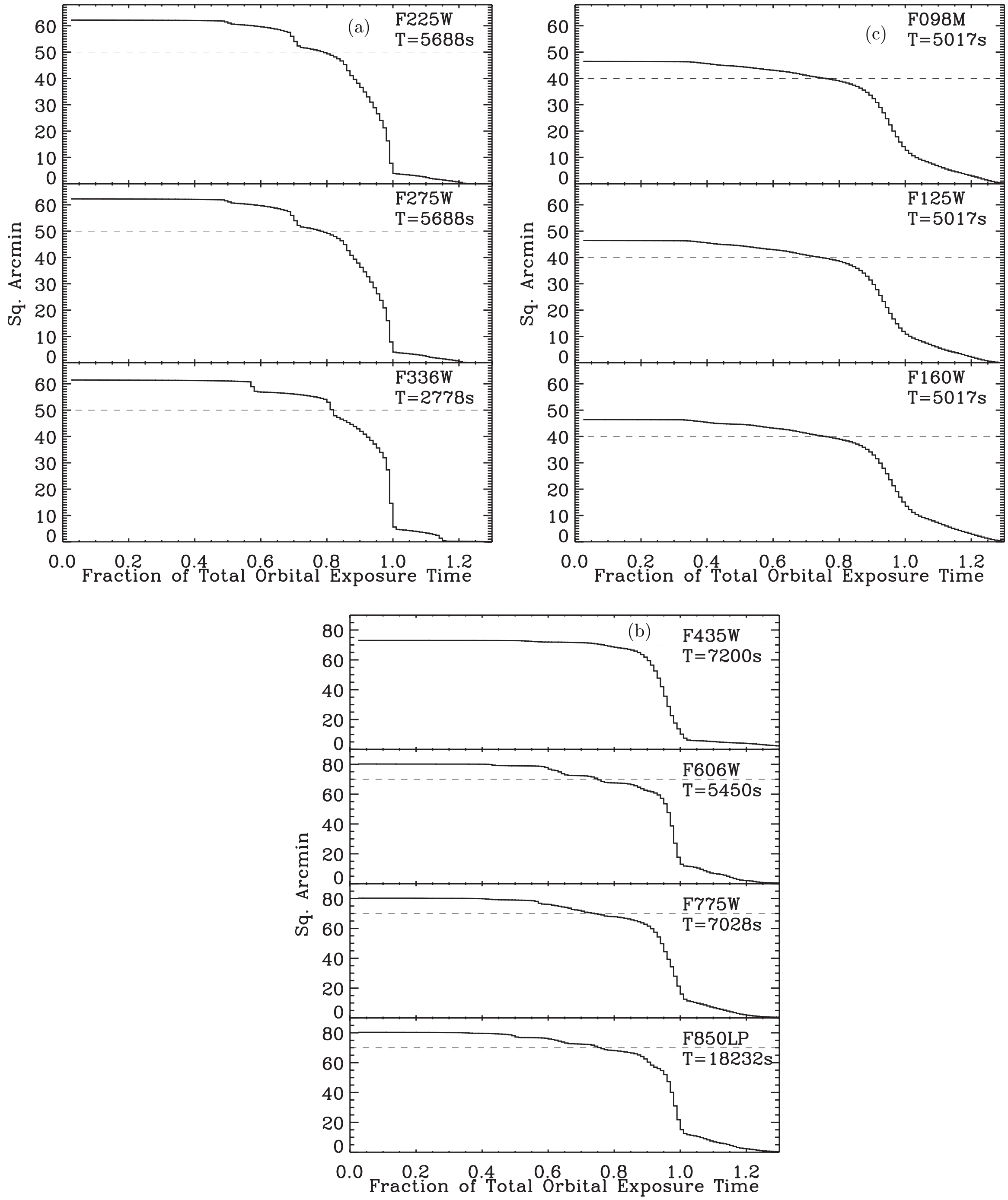

Figure 8. (a) Cumulative distribution of the maximum pixel area that has the specified fraction of total orbital exposure time in each ERS UVIS mosaic. These effective areas must be quantified in order to properly do the object counts in Figure 11(a). (b) Same as Figure 8(a), but for the GOODS v2.0 mosaics in *BViz*. (c) Same as Figure 8(a), but for the ERS mosaics in the WFC3 IR filters.

appear much smoother in the IR and more clumpy in the UV, which occurs due to the specific distribution of their young and old stellar populations as well as their dust (see Windhorst et al. 2002 for a discussion of this effect for all Hubble types). Hence, star-forming regions in well-resolved galaxies can be deblended into separate objects by SExtractor if the deblending is overly aggressive. Fortunately, most of these intermediate-redshift galaxies are not bright in the observed UV, causing the UVIS fields to appear rather sparse, and making deblending a minor issue.

The UVIS images have a less uniform background (∼10%–15% of sky), which as discussed in Section 4.1.1 can possibly be improved, when accurate on-orbit UVIS sky flats have been accumulated over time. For these reasons, we adopted a seemingly low threshold for object detection with SExtractor, requiring 4 connected pixels that are 0.75σ above the background in the UV. Due to the clumpy nature of the ERS objects in the UV, we convolved the UVIS image with a Gaussian kernel of FWHM of 6.0 pixels for the object detection phase only. The deblending parameter, DEBLEND_MINCONT, was set to 0.1, to assure that real objects were not overdeblended. It should be emphasized that object crowding is *not* an issue in these medium depth UV images (e.g., Windhorst et al. 2008), so that the use of a larger SExtractor convolution filter, a lower

SB-detection threshold, and less object deblending is fully justified. The 6.0 pixel Gaussian convolution kernel improves the SB sensitivity by ∼2 mag, given that the low-level UV sky gradients occur over much larger spatial scales than the typical faint galaxy sizes (see Sections 4.1 and 5.5). Together with the fact that the UVIS catalogs were made with SExtractor in dual image mode—using the much deeper ACS *B*-band image as the detection image, as described above—avoids excessive deblending of the very clumpy UV objects, which limits the number of spurious UV objects detected, as shown in the discussion of the ERS catalog reliability in Section 5.3.

The SExtractor input parameters for the ACS images and WFC3/IR images were the same. The detection threshold was set to 1.5σ, again requiring 4 connected pixels above the threshold for catalog inclusion. The convolution filter was a Gaussian with FWHM of 3.0 pixels, and DEBLEND_MINCONT was set to 0.06. For all 10 bands, the appropriate weight maps (see Section 4.2.2) were used in order to correctly account for image borders (Figure 3), as well as to properly characterize the photometric uncertainties and the effective areas for each mosaic (see Figures 8(a)–(c)).

5.2. Object Extraction

Two post-processing steps were taken to clean the catalogs of residual artifacts. First, due to the relatively small number of exposures per ERS filter, there were residual cosmic rays at the borders of the dither patterns, and in the chip gaps. These were cleaned by masking out all objects in regions where the number of exposures was less than three. Therefore, the total area coverage in each filter (Table 2 and Figures 8(a)–(c)) is slightly different. Second, SExtractor will detect the diffraction spikes of bright point sources. These are removed by searching for bright objects with FWHM near the size of the PSF and searching for surrounding objects in the catalog that are *both* highly elongated *and* oriented radially outward in sets of four from that compact object. Since the number of bright stars is not large (see Section 4.3.2 and figures therein, Sections 5.5 and 6.1), this is only a minor correction to the catalog, and only a few dozen diffraction spikes were found by SExtractor and removed in this way.

Magnitudes were all measured on the AB scale using the most current zero points available on the WFC3 Web site, which are listed in Table 2. Both Petrosian (1976) magnitudes were measured using a Petrosian factor of 2.0, and Kron (1980) magnitudes were measured using a Kron factor of 2.5 (SExtractor parameter MAG_AUTO). For the galaxy counts in Section 7.2, Kron magnitudes were used, because the correction to total magnitude—preferably using a Sersic extrapolation—is less than that typically required for a Petrosian magnitude. Within the errors, the Kron and Sersic based number counts are indistinguishable (Hill et al. 2011). The total magnitude errors in the ERS as a function of total AB magnitude were determined from the SExtractor errors in each filter, which are a combination of the MultiDrizzle RMS-map errors and the image shot noise.

5.3. ERS Catalog Reliability

To test the reliability of ERS object catalogs, we performed the negative image test (cf. Yan & Windhorst 2004). In brief, all 10 ERS mosaics were multiplied by –1.0, and then SExtractor was run with exactly the same parameters as the object finding procedure in Sections 5.1 and 5.2. This test showed that our ERS catalog generation was conservative due to the combination of several factors. These include drizzled the larger mosaic pixel size of 0.″090, the requirement of *four* connected pixels above the detection threshold, and the sizes of the Gaussian filters applied in the object detection phase. The choice of the SExtractor parameters listed in Sections 5.1 and 5.2 were determined by trial and error to create the most reliable catalogs at each wavelength.

In fact, these SExtractor parameter settings yielded *no plausible* spurious detections when it was run on the 10 negative ERS images. In total, only six negative "objects" were found, but these were all on the image borders, and the real ERS object catalogs were similar cleaned of such border defects. *If* the noise in the ERS images were completely Gaussian, then at the $\gtrsim 5\sigma$ detection limit we would expect that 2.9×10^{-7} of the $6500 \times 3000/4$ independent ERS pixels (see Figure 5(a)) would yield a bogus object, or ∼1.4 bogus object in the combined 10-band catalog (the grand union) of 22,000 ERS objects. This is consistent with no convincing bogus objects found in the 10 negative ERS images after discarding the image borders. This exercise shows that at the 5σ 50% completeness level (see also Figure 9 below), our ERS object catalogs are $\gtrsim$99.97% reliable. In astrophysical data samples, a compromise always has to be sought between sample reliability and sample completeness, while ideally maximizing the sum of the two (Windhorst et al. 1984a). The reason we choose here to have essentially 100% reliable catalogs—at the expense of some catalog incompleteness below—is the existence of the deeper optical–near-IR ACS and WFC3 images in the HUDF (Beckwith et al. 2006; Bouwens et al. 2010b; Yan et al. 2011b) in the $BVizY_sJH$ filters. These images made digging deeper into the ERS image noise unnecessary. Instead, the faint end of the galaxy counts at AB $\gtrsim$ 26–27 mag in Section 7 will be derived in $BVizY_sJH$ from these HUDF images, which is in roughly the same direction of the sky.

5.4. ERS Catalog Completeness

Figure 9 shows the sample completeness functions of the 10-band ERS images. These were derived by Monte Carlo insertion of faint point sources into the ERS images, and plotting the object recovery ratio as a function of total magnitude. Most faint galaxies observed by *HST* are slightly resolved at the *HST* diffraction limit (e.g., Cohen et al. 2003; Hathi et al. 2008; Windhorst et al. 2008), so that for faint galaxies these limits are slightly brighter than for point sources, as discussed in Section 7.2 and shown in Figure 10(a).

In summary, the WFC3 UVIS images are ∼50% complete for point-like objects with $\gtrsim 5\sigma$ detections in total flux for AB $\simeq$ 26.3 mag in F225W, AB $\simeq$ 26.4 mag in F275W, and AB $\simeq$ 26.1 mag in F336W. The WFC3 IR images are ∼50% complete to AB $\simeq$ 27.2 mag in F098M, AB $\simeq$ 27.5 mag in F125W, and AB $\simeq$ 27.2 mag in F160W, as listed in Table 1. The multi-year GOODS ASC/WFC v2.0 images in $BViz$ are substantially deeper than this, and reach AB $\gtrsim$ 27.5 mag in general. The actual star counts in Section 6 appear indeed complete to roughly these limits in the UV, but to slightly brighter limits in the IR due to the increasing object confusion of red stars with faint red background galaxies (see the figure in Section 5.5).

The actual UV galaxy counts in Section 7.2 turn over at a level rather close to the above UVIS point-source sensitivity limits. This is due to the generally more compact nature of the ERS objects, and the extremely faint zodiacal sky background in the UV. In the IR, the galaxy counts turn over at levels a little brighter than the 5σ point-source sensitivity limits listed in

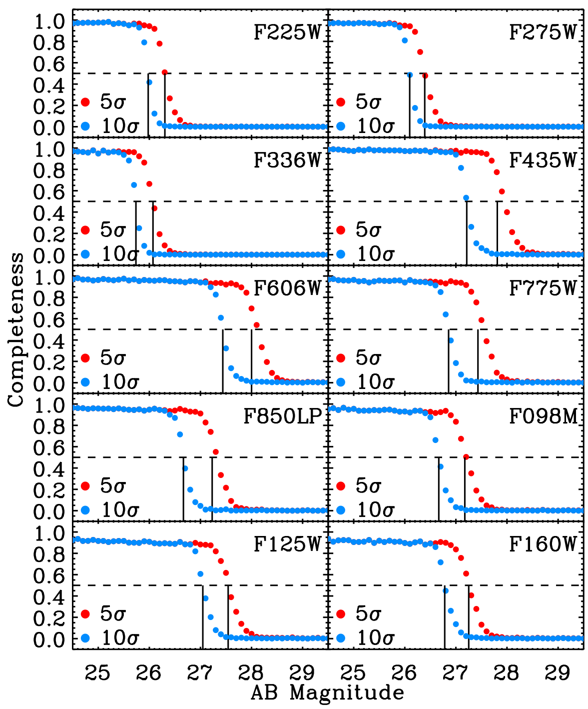

Figure 9. Panchromatic completeness functions of the number counts in the panchromatic ERS images at the 5σ (red) and 10σ (blue) detection levels of total object magnitudes. These were derived by Monte Carlo insertion of faint point-like objects into the ERS images, and plotting the object recovery ratio as a function of total magnitude. At the $\gtrsim 5\sigma$ level, the ERS is more than 50% complete at levels fainter than AB ∼ 26 mag for the WFC3 UVIS images, fainter than AB ∼ 27 mag for the WFC3 IR images, and substantially fainter than AB ∼ 27 mag for the deeper multi-year GOODS ACS v2.0 images (see Table 1).

(A color version of this figure is available in the online journal.)

Table 2. This is due to the higher zodiacal sky-background values in the near-IR (see Table 2), combined with their somewhat larger sizes at the longer wavelengths (Section 5.5 and figures therein; see also Windhorst et al. 2002), even though faint red field galaxies selected in Y_sJH are in general still rather compact. Object confusion at these flux levels is relatively modest, especially at the *HST* diffraction limit, although natural confusion—which due to the intrinsic object sizes and *not* the instrumental PSF FWHM—becomes increasingly important at fainter fluxes (AB $\gtrsim$ 25 mag; e.g., Windhorst et al. 2008).

In summary, the point-source sensitivity of our ERS catalogs is described by the simulations in Figure 9. The corresponding 50% point-source completeness limits are listed in Table 1. The actual observed panchromatic star counts (Section 6.1 and figures therein) are complete to roughly the 5σ limits of Figure 9 in the WFC3 UVIS filters, and to the 10σ limits of Figure 9 in the ACS $BViz$ and WFC3 IR filters.

Rather than repeating the object simulations of Figure 9 to assess the actual completeness limits for the slightly extended galaxies (see Section 5.5 and figures therein), in Section 7 below we take a different and more empirical approach of determining the ERS incompleteness for faint galaxies by directly comparing the panchromatic ERS galaxy counts to AB $\lesssim$ 25.5–27 mag to the galaxy counts in the much deeper, but adjacent HUDF field. Since the effects of cosmic variance are relatively small over the 4′ separation between the ERS and HUDF fields (see Section 7 and Figure 3), this comparison directly shows that the ERS catalogs are approximately $\gtrsim$50% complete for samples of compact galaxies (see Section 5.5) to flux levels that are approximately 0.5–1.0 mag brighter (from the UVIS to the IR) than the ERS stellar samples in the same filters.

5.5. Star–Galaxy Separation in the ERS Mosaics

Stars and galaxies were separated as follows. In each filter, the stellar locus was defined as shown in the usual plot of the object FWHM versus total AB magnitude (e.g., Cohen et al. 2003). Figure 10(a) illustrates our star–galaxy separation procedure used for the 10-band ERS images. Objects with FWHM < PSF FWHM (from Table 2) are image defects, bad pixels, and some remaining CRs. Hence, objects to the left of the black vertical lines plotted at FWHM $\simeq$ 0″.07–0″.15 are *smaller* than the PSF, and are discarded. Objects in the thin vertical filaments immediately larger than this are stars (plotted as thin reds dots in Figure 10(a)), and they in general have PSF FWHM $\lesssim$ FWHM $\lesssim (1+\epsilon) \times$ PSF FWHM, where $0 \lesssim \epsilon < 1$. Figure 10(a) shows that ERS stars straddle the instrumental PSF FWHM to AB $\simeq$ 27 mag. Objects to the right of the black dashed slanted lines are galaxies, and they in general have FWHM $\gtrsim (1+\epsilon) \times$ PSF FWHM, where "$1+\epsilon$" is a weak function of total S/N, as shown by the two solid slanted lines in each of the panels in Figure 10(a).

Next, all 10 independent ERS object catalogs—each with their independent star–galaxy separation and photometry—were merged by astrometric cross-matching. In order to maximize the 10-band information, we considered an object to be a star if it was classified as stellar in at least 3 out of 10 ERS filters. This provides robust stellar classifications, perhaps to fainter limits than can be done in single filter alone.

From Figure 10(a), we can see that the stars separate out well from the galaxies to about AB $\simeq$ 25.5–26.0 mag, and somewhat fainter in the ACS $BViz$ filters and the WFC3 IR filters. To these flux levels, the star counts follow a power law rather well, as shown in Section 6.1. The choice to require an object to be classified as a star in three filters—as opposed to all 10 filters—was made because stars can be either very red or sometimes very blue, and so stars are often not detected in all 10 ERS filters. Also, we are merging the data from three different *HST* instruments and detectors (WFC3 UVIS CCD, ACS/WFC CCD, and the WFC3 IR detector), so subtle PSF and sampling differences between these instruments can lead to the misclassification of a faint star in some of the 10 ERS filters, depending on its color. Since brighter stars are always seen at least in three (adjacent) ERS filters, we require all of the fainter stars to be classified as stellar in at least three of the ERS filters as well.

5.6. Confirmation of Star–Galaxy Separation: Proper Motion and Stellar Colors

As shown in Section 4.3.2 and Figure 4(c), all ERS objects together—which are $\gtrsim$97.8% galaxies—allowed us to bring the WFC3 UVIS and IR coordinate system on average on top of the ACS WFC WCS to within 0.4–0.5 mas in both R.A. and decl. After having done this, the 4511 ERS objects classified as galaxies show indeed no significant residual motion over 5.97 years. However, for all 103 ERS objects classified as stars, an *average* proper motion of 2.30–2.02 mas yr^{-1} was detected at the 4.1σ–5.8σ level in R.A. and decl., respectively (see Section 4.3.2). For at least 32 out of the 103 ERS stars, this proper motion was discovered *individually* at the $\geqslant 3\sigma$ level (see Figure 4(c)). The total *average* proper motion of all 103 ERS stars on the sky is 3.06 mas yr^{-1}, summed in quadrature over the

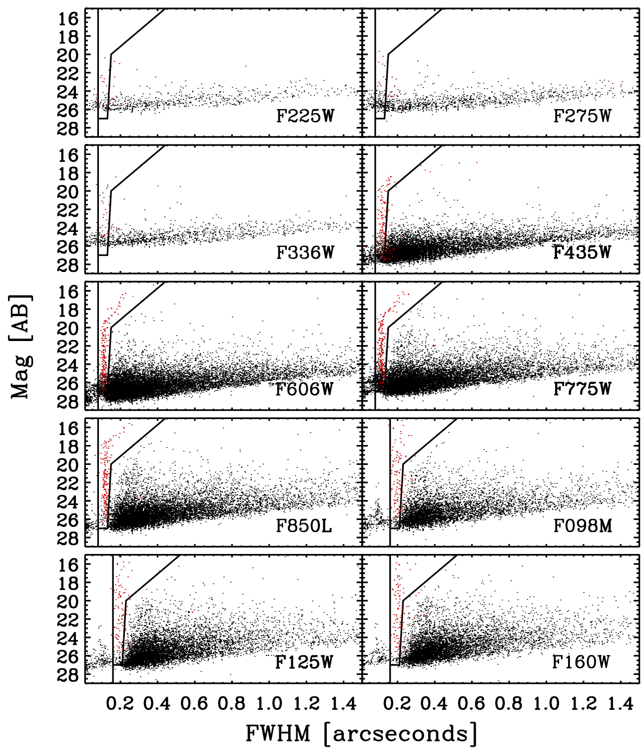

(a)

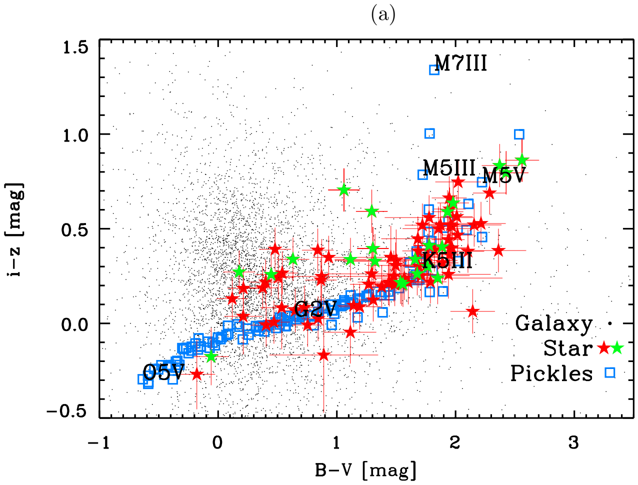

(b)

Figure 10. (a) Panchromatic star–galaxy separation in the 10-filter ERS images. Plotted are object total AB magnitude vs. SExtractor image diameter FWHM (FWHM $\simeq$ twice its half-light radius). Objects with image diameter $\lesssim 0.9 \times$ PSF FWHM—where the PSF FWHM ($\simeq 0\farcs07$–$0\farcs15$) is from Table 2—are image defects (black dots). Objects in the thin vertical filaments (red dots) immediately larger than this are classified as stars. ERS stars were defined to be those objects that resided in this red area in at least 3 out of 10 ERS filters. Objects to the right of the full-drawn slanted lines are galaxies (black dots). The star–galaxy separation becomes less reliable for fluxes fainter than AB $\simeq$ 26–27 mag in UV$BVizY_sJH$, respectively. Details are discussed in the text. (For best display, please zoom in on the full-resolution version of this image, which is available on http://www.asu.edu/clas/hst/www/wfc3ers/ERS2_gxysv4ln.tif.) (b) The $(i-z)$ vs. $(B-V)$ color–color diagram in the GOODS $BViz$ filters for all ERS galaxies (black dots) and stars (red and green asterisks). These are compared to the Pickles (1998) model stellar SED library (blue squares), which range in spectral type from O5V to M7V, and also show the giant branch models up to type M7III. The observed ERS stellar colors are shown with their 1σ error bars. Only stars with combined color errors along each axis $\lesssim$0.5 mag are plotted. Green asterisks mark ERS stars with proper motion established at the $\gtrsim 2\sigma$ level.

(A color version of this figure is available in the online journal.)

R.A. and decl. proper motions. The mean error is 0.66 mas yr^{-1}, which amounts to a 4.6σ detection of the overall ERS stellar proper motion. The dispersion on this number in Figure 4(c) is 6.70 mas yr^{-1}. We will interpret these numbers in more detail below. In conclusion, while ERS proper motions *alone* cannot confirm that *all* our ERS objects classified as stellar are in fact Galactic stars, *average* stellar proper motion *is* detected at high significance level for the *entire sample* of 103 ERS stellar candidates, making it in retrospect likely that most of these are in fact Galactic stars.

The ERS colors in Figure 10(b) are more conclusive in supporting our ERS star–galaxy separation procedure a posteriori. Figure 10(b) shows the $(i-z)$ versus $(B-V)$ color–color diagram in the GOODS filters, where all ERS objects have the highest S/N (see Figure 9). ERS objects classified as galaxies as shown as black dots, and ERS objects classified as stars with green or red asterisks. Green asterisks mark ERS objects that show proper motion at the $\geqslant 3\sigma$ level in Figure 4(c) (see Section 4.3.2). The $(i-z)$ versus $(B-V)$ colors are compared to the Pickles (1998) model library SEDs (blue squares), which range in spectral type from O5V–M7V, and also show giant branch models up to M7III. The observed ERS stellar colors are shown with their 1σ error bars. Only stars with combined color errors along each axis $\lesssim$0.5 mag are plotted. It is clear that within the errors, most stellar ERS objects have colors of K–M type main-sequence stars, although there are a few ERS stars with color as blue as BV–GV types.

There are about 20 ERS stars in the color range $0 \lesssim (B-V) \lesssim 1.4$ mag with $(i-z)$ colors $\gtrsim$0.3 mag redder than the Pickles (1998) main sequence. At least eight of these also have significant proper motion at the $\gtrsim 3\sigma$ level, and are thus real Galactic stars. All 20 objects significantly redder than the Pickles (1998) main sequence were inspected by eye and correlated with other data. Three have VLT redshifts: one is a Seyfert galaxy at $z = 1.031$ in a group with similar spectroscopic redshifts, the other a compact elliptical at $z = 0.251$ next to a very faint stellar object, and the third is a stellar object next to an object at $z = 2.217$ with a neighbor at a similar redshift. The latter two stellar objects also have significant proper motion, and are likely real Galactic stars that are very close to an extragalactic object whose VLT redshift was actually measured.

Thus at least 17—and likely 19—of these 20 ERS stars with colors significantly redder than the Pickles (1998) main sequence have either significant proper motion and/or clear stellar morphology. Many of these appear to be stars that were unavoidably saturated in the ERS images. Because both their colors are $\gtrsim$0.0 mag—they have higher ADU in i band than in z band, and in V band than in B band—given the ACS/WFC QE curve. Hence, their measured $(i-z)$ flux will be too red, and their $(B-V)$ color slightly too blue. Since these stars are saturated in nearly every ACS exposure, more accurate colors cannot be determined with the current mosaics, and their appearance above the Pickles (1998) main sequence does thus not rule them out as stars. Some of the reddest stars well away from the Pickles (1998) main sequence could be asymptotic giant branch stars with surrounding dust shells that could considerably redden their $(B-V)$ and $(i-z)$ colors significantly.

We also need to address how many of the stellar objects that are within the errors consistent with the Pickles (1998) stellar main sequence could be compact background galaxies. Figure 10(b) shows that the $(i-z)$ versus $(B-V)$ color space of zero-redshift stellar SEDs overlaps somewhat with the colors of intermediate-redshift galaxies, which largely occupy the region $(B-V) \lesssim 1$ mag *and* $(i-z) \gtrsim 0.15$ mag. This is a limitation of the current color confirmation of the stellar ERS candidates.

Only multi-parameter 10-band SED fitting of *all* ERS objects can address this issue more fully, which we will address in a future paper (Cohen et al. 2011). However, the available VLT spectra can give us some idea.

Among the 103 objects classified as ERS stars, many would have been bright enough to have been included in the VLT redshift survey, which is complete to AB $\lesssim$ 24 mag, but covered objects as faint as AB $\lesssim$ 25 mag. Among the 103 stellar ERS objects, 11 appear to be compact extragalactic objects confirmed to have VLT redshifts $z > 0$. One of these is a quasar with an underlying early-type galaxy at $z = 0.734$.

In summary, this detailed study in Figure 10(b) confirms that at least 90–92 of the 103 stellar ERS objects have either significant proper motions (Figure 4(c)), stellar colors consistent with the Pickles (1998) main sequence (Figure 10(b)), and/or are not extragalactic objects with VLT redshifts $z > 0$. Conservatively, we can thus conclude that our ERS stellar objects are indeed Galactic stars with $\gtrsim$87% reliability. This provides a posteriori confirmation that our ERS star–galaxy separation method of Section 5.5—which was based on measured effective image diameters *only* (Figure 10(a))—is indeed valid. This then also means that we may consider the statistical proper motions of all ERS stars in Figure 4(c), to investigate if the implied *average* proper motion shows us something interesting about Galactic structure of very faint stars at high Galactic latitude (the GOODS-South field has $b^{II} = -54°$). We discuss this in Section 6 in more detail.

As a final remark, ideally one would like the star–galaxy separation procedure to also include accurate fits of a library of (redshifted) SEDs to the 10-band ERS object photometry, and so help decide whether an object is most likely a zero-redshift star or a redshifted galaxy. This is beyond the scope of the current paper, and is pursued by Cohen et al. (2011) for the ERS stars and galaxies separately. This paper will also attempt to do a stellar + power-law AGN SED fits to *all* ERS objects, including on a pixel-to-pixel basis. This procedure will also provide better estimate of the AGN contamination of the ERS sample, rather than relying on the presence of weak point-like components in the ERS images alone. Suffice to say here that in Figure 10(b) most ERS stars have colors consistent with the stellar main sequence, so that contamination of our *stellar* ERS objects by weak AGN or other compact extragalactic objects is likely small. This is confirmed by the high proper motion stars in Figure 10(b), which have statistically the same color distribution as the stellar ERS objects without measurable proper motion.

6. RESULTS ON ERS STARS

6.1. The Panchromatic ERS Star Counts to AB $\simeq$ 26 mag

Figure 11(a) shows the differential panchromatic star counts in the 10-band ERS images. The star–galaxy separation breaks down at fluxes AB $\gtrsim$ 26 mag in $BVizY_sJH$. However, for AB $\gtrsim$ 22 mag galaxies outnumber stars by a large margin, so the more uncertain star–galaxy separation for AB $\gtrsim$ 26 mag will not affect the quality of the galaxy counts. The star counts, of course, become correspondingly harder to do for AB $\gtrsim$ 25 mag, and so in Section 6.2 and Figure 10(b) additional criteria such as colors and proper motion were used to confirm faint stars at higher confidence.

The solid black line in the F850LP panel of Figure 11(a) represents the spectroscopic star counts to AB $\simeq$ 25 mag from the *HST* Cycle 14 ACS grism survey "PEARS" (Probing Evolution And Reionization Spectroscopically) of Pirzkal et al. (2009). Since for these objects we can use the low-resolution ACS G800L spectroscopic data as independent confirmation of their stellar nature, they have higher accuracy than the image-based star counts alone. The southern PEARS ACS grism survey was done over a similar sized area to the ERS, covering an overlapping portion of GOODS-S. Hence, it is encouraging that the Pirzkal et al. (2009) grism star counts, which are for spectral types of $M0$ and later, have the same *slope* as our direct-imaging ERS star counts in F850LP. The slightly different star count *amplitude* for the flux range 18 mag $\lesssim$ AB $\lesssim$ 25 mag is likely due to the fact that the spectroscopic sample was limited to later spectral types, where those grism classifications were most reliable. The good agreement in star counts between the two different survey methods confirms that—as far as faint stars are concerned—our star–galaxy separation is accurate to about AB $\simeq$ 25 mag.

Figure 11(b) shows the ERS star count slope versus observed wavelength in the flux ranges AB $\simeq$ 19–25.5 mag for the three UV WFC3 filters, AB $\simeq$ 16–26 mag for the GOODS/ACS $BViz$ filters, and AB $\simeq$ 15–25 mag for the three WFC3 IR filters, respectively. The *GALEX* FUV and NUV points of Xu et al. (2005) are also plotted at 153 and 231 nm, and cover the flux range AB $\simeq$ 17–23 mag, using primary color criteria to accomplish star–galaxy separation at the 4″–66″ FWHM *GALEX* resolution. The statistics of the star counts in the three bluest ERS filters (F225W, F275W, and F336W) are rather sparse (Figure 11(a)). As a consequence, our three bluest best-fit ERS power-law slope values are rather uncertain, as indicated by the larger error bars in Figure 11(b). The *GALEX* FUV and NUV star count points of Xu et al. (2005) are complete to somewhat brighter levels (AB $\simeq$ 23–24 mag), but have much better statistics. As a consequence, the *GALEX* FUV and NUV star count slope points in Figure 11(b) have smaller error bars, and at the common wavelength of ~230 nm they therefore carry larger weight than the ERS star count slope in the mid-UV.

Given these uncertainties, the Galactic star count slope at the faint end is remarkably flat at all wavelengths from the Balmer break to the near-IR, although it is rather poorly determined from the ERS data alone below the Balmer break. The values of the best-fit ERS power-law star count slope is in general of order 0.03–0.05 dex mag^{-1}. Including the more accurate *GALEX* star count slope values at 150 and 230 nm, the panchromatic faint end of the star-count slope appears to be always in the range 0.03–0.20, i.e., at all ERS wavelengths the faint star-count slope remains well below Euclidean value of 0.6 dex mag^{-1}. This shows that to a depth of AB $\simeq$ 25–26 mag at all wavelengths in the range 0.2–2 μm, the ERS images readily penetrate through most of the thick disk of our Galaxy at these latitudes ($b^{II} \simeq -54°$) in the direction of the Galactic anti-center ($l^{II} = 224°$; Ryan et al. 2005; Beckwith et al. 2006). This trend was also seen in the red ACS imaging parallels of Ryan et al. (2005), and the red ACS GRAPES and PEARS grism observations of Pirzkal et al. (2005, 2009), respectively, each of which constrained the scale height of Galactic L and T dwarfs to about 300–400 pc.

In the bluest three WFC3 filters F225W, F275W, and F336W, the WFC3 ERS finds only 22, 18, and 27 faint stellar candidates, respectively. Most of the full sample of ERS stars have 10-band colors red enough to indicate Galactic halo K–M type stars and possibly a few L and T dwarfs, but a few of the faint stars are blue (see Section 5.6 and Figure 10(b)). The latter could be faint Galactic white dwarfs, though there were no UV detected stars that were not also seen in the ACS B band. The effective ERS UV stellar detection limit of AB $\simeq$ 25 mag could trace

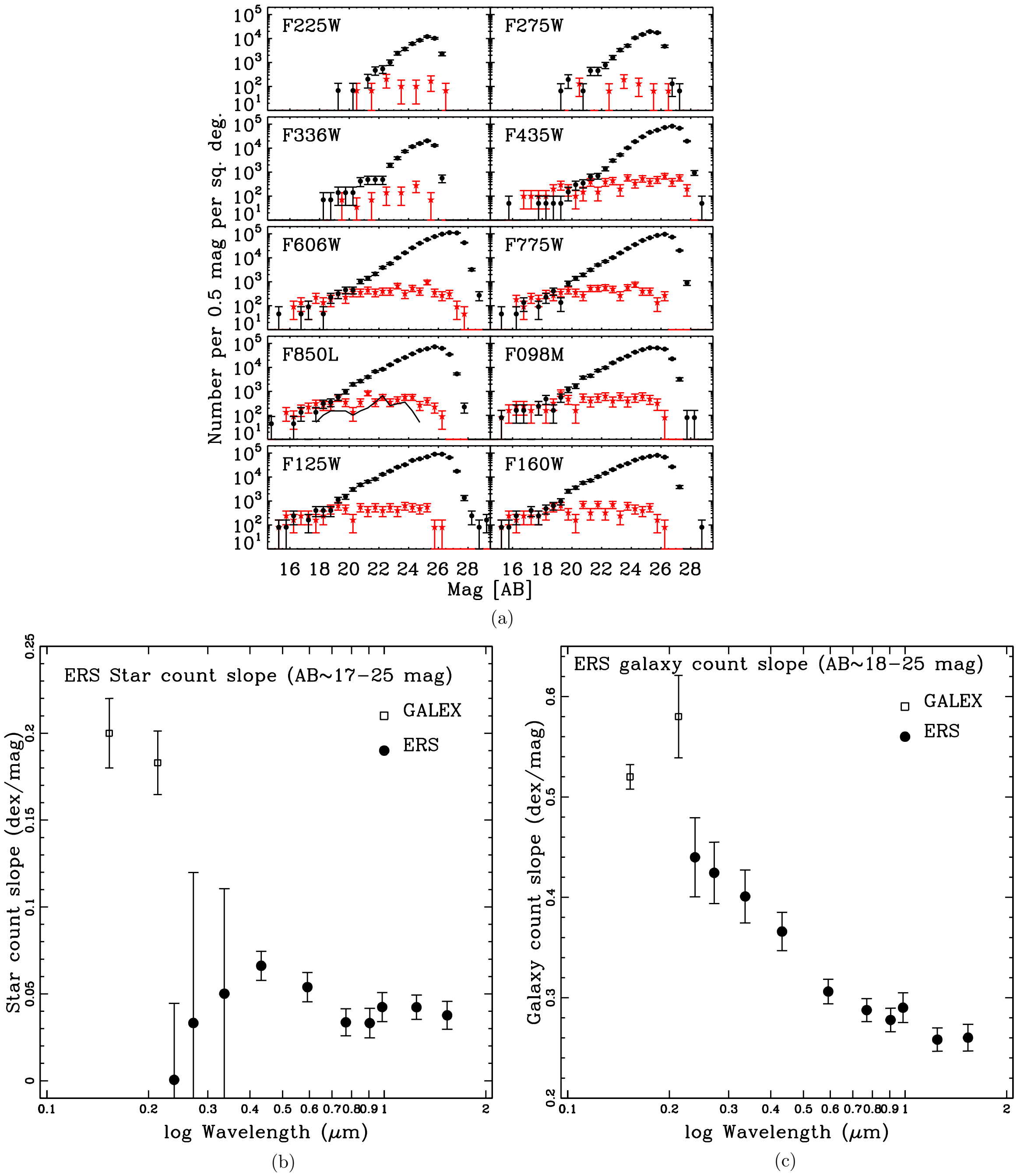

Figure 11. (a) Differential panchromatic star counts (red asterisks) and differential panchromatic galaxy number counts in the ERS images (black dots), with the optimized star–galaxy separation from Figure 10(a). All 10 ERS filters are shown in units of object numbers per 0.5 mag deg^{-2}, but in the three bluest filters (F225W, F275W, and F336W) some of the brightest bins were doubled to 1.0 mag in width to improve statistics. The solid black line in the F850LP panel are the spectroscopic star counts from the *HST* PEARS ACS grism surveys of Pirzkal et al. (2009), which are in good agreement with our F850LP star counts. (b) ERS Star count slope (filled circles) versus observed wavelength in the flux ranges AB $\simeq$ 19–25.5 mag for the three UV WFC3 filters, AB $\simeq$ 16–26 mag for the GOODS/ACS $BViz$ filters, and AB $\simeq$ 15–25 mag for the three WFC3 IR filters, respectively. The faint end of the Galactic star count slope is remarkably flat at all wavelengths from the mid-UV to the near-IR, with best-fit power-law slopes in general of order 0.03–0.20 dex mag^{-1}. The two bluest points at 153 and 231 nm are from the *GALEX* star counts of Xu et al. (2005; open squares), which cover AB = 17–23 mag. The ERS counts at the shortest wavelength suffer from small number statistics and so are less reliable (see Figures 10(a) and 11(a)). For further details, see the text. (c) ERS Galaxy count slope (filled circles) vs. observed wavelength in the flux ranges AB $\simeq$ 19–25 mag for the three UV WFC3 filters, AB $\simeq$ 18–26 mag for the GOODS/ACS $BViz$ filters, and AB $\simeq$ 17–25 mag for the three WFC3 IR filters, respectively. The two bluest points at 153 and 231 nm are from the *GALEX* galaxy counts of Xu et al. (2005; open squares), which cover AB = 17–23 mag. The galaxy counts show the well known trend of a steepening of the best-fit power-law slope at the bluer wavelengths, which is caused by a combination of the more significant *K*-correction and the shape of the galaxy redshift distribution at the selection wavelength.

(A color version of this figure is available in the online journal.)

a $T = 2 \times 10^4$ K white dwarf with an absolute magnitude in the range $M_{\rm bol} \simeq +15$ to +10 mag (Harris et al. 2006) out to a distance of 1–10 kpc, respectively, assuming modest bolometric corrections. The faint stellar objects in the 10-band ERS data are obviously of great interest by themselves and will be studied in more detail in a future paper. An important lesson learned for UV observations of high-latitude fields is that there are so few UV bright stars, that one has to ensure that individual exposures are long enough in order to align and drizzle (or stack) them using faint galaxies. In the ERS UV images we did this using the cross-correlation technique, as explained in more detail in Appendix A.

6.2. The Nature of Faint ERS Stars from Proper Motion and Stellar Colors

Figure 10(b) suggests that the majority of ERS stars have red colors characteristic of faint red main-sequence stars. Their typical spectral type is in the range K0V–M5V with an average spectral type of ∼K5V. For these stars, the expected M_V ranges from +5.8 to +12.3 mag with an average of M_V ∼+8 mag. With the flat ERS star count slope of Figure 11(a), the *average* ERS star has an AB magnitude of ∼23 mag, while the ERS stellar detection limit is AB $\lesssim$ 26 mag. Hence, the *average* faint red ERS star will be at a distance of about $R \simeq 10$ kpc from the Sun. The direction of the GOODS-South field at R.A. = $03^h32^m39^s$, decl. = $-27°47'29''.1$ is in the Southern Galactic hemisphere, about 54° below the plane of the Milky Way, and in the general direction of the Galactic anti-center. Stars in this direction at ∼10 kpc distance from the Sun will thus be bulge and disk stars ∼8 kpc below the Galactic plane, i.e., well below the outer Orion arm of the Galaxy. At this distance, the above *average* ERS proper motion of 3.06 ± 0.66 mas yr^{-1} amounts to an average stellar *tangential* velocity of $\lesssim$145 ± 31 km s^{-1} (m.e.). These stellar velocities and their dispersion are in part due to the projected solar motion in the sky—compared to the Galactic Local Standard of Rest—and in part due to the true space velocities of ERS stars in the Galactic bulge and disk. While a detailed discussion of the proper motion of ERS stars and its implication for Galactic structure is beyond the scope of the current paper, we will here briefly discuss how our ERS proper motion results compare to previous proper motion and radial velocity observations of the Galactic bulge and disk at intermediate to high Galactic latitude.

A proper motion study to $V \lesssim 22.5$ mag at the North Galactic Pole by Majewski (1992) shows a systemic velocity of −120 km s^{-1} at the edge of the thick disk ($z \gtrsim 5.5$ kpc). Clarkson et al. (2008) show similar proper motion values at $R \sim 5$ kpc, but in Baade's window from multi-epoch *HST*/ACS images that are effectively complete to about $I \lesssim 21$ mag given the more crowded images at low Galactic latitudes. Kinman et al. (2007) find that Galactic Blue Horizontal Branch stars with an average distance to the Galactic plane of $z \lesssim 8$ kpc have zero galactic rotation and roughly isotropic velocity dispersions of 93–81 km s^{-1} in the tangential and z directions, respectively, or ∼123 km s^{-1} in the plane of the sky. Theoretical disk+bulge+halo models (Battaglia et al. 2005; Klypin et al. 2002) predict velocity dispersions at $R \sim$ 5–10 kpc of 150 km s^{-1} for the Galactic bulge+thick disk components.

These values are very similar to the 145 km s^{-1} value implied from the *average* proper motion observed for our faint red ERS stars at relatively high Galactic latitude ($b^{II} = -54°$). In other words, the Galactic (thick disk+bulge) velocity dispersion *implied* from our faint red ERS stellar proper motions is consistent with these previous observations and theoretical model predictions. It is worth noting, however, that these previous observations are based on high-resolution radial velocities *and* proper motions of Galactic stars with $V \lesssim 16$ mag, or proper motions alone for stars with $V \lesssim 22.5$ mag. Our ERS observations push this substantially fainter for proper motions at high Galactic latitudes, to flux levels (AB $\lesssim$ 25–26 mag) where *high* resolution spectroscopy cannot be done with current ground based facilities. Systematic proper motion studies of very faint stars at *HST* resolution at high Galactic latitudes thus have the potential to sample part of Galactic structure that is otherwise not easily accessible. This topic will be studied in further detail in a subsequent paper.

7. RESULTS ON GALAXIES IN THE ERS

7.1. The Panchromatic ERS Galaxy Counts to AB ≃ 26–27 mag

Figure 11(a) also shows the differential panchromatic galaxy number counts in the 10-band ERS images. *No* completeness corrections—as implied by Figures 9 and 10(a)—were applied to the faint end of the panchromatic ERS galaxy counts in Figure 11(a). Instead, to be conservative, the data points are not plotted in all panels of Figure 12 at the flux level where the counts clearly start to deviate from a best-fit faint-end power law (see Figures 11(a) and (c)) by more than 50%. This in general occurs 0.5–1.0 mag brighter than the 50% point-source completeness limits listed in Table 1, as derived from Figure 9.

Figure 11(c) shows the ERS galaxy count slope versus observed wavelength in the flux ranges AB ≃ 19–25 mag for the three UV WFC3 filters, AB ≃ 18–26 mag for the GOODS/ACS $BViz$ filters, and AB ≃ 17–25 mag for the three WFC3 IR filters, respectively. The *GALEX* FUV and NUV points of Xu et al. (2005) are also plotted at 153 and 231 nm, and cover AB = 17–23 mag, again using primary color criteria to accomplish star–galaxy separation at the 4″–6″ FWHM *GALEX* resolution. The statistics of the galaxy counts in the three bluest ERS filters (F225W, F275W and F336W) are sparse (Figure 11(a)), and at the *bright-end* the ERS object definition and deblending is more complex given the sizes of the brighter objects (Figure 10(a)). As a consequence, the best-fit ERS galaxy count power-law slope values become somewhat more uncertain at the bluer ERS wavelengths (Figure 11(c)). The *GALEX* FUV and NUV galaxy counts of Xu et al. (2005) are complete to somewhat brighter levels (AB ≃ 25 mag), but have much better statistics than the ERS. Given the much larger size of the *GALEX* beam (4″–6″ FWHM), they do however suffer from more uncertain star–galaxy separation, which for *GALEX* needed to be done by using multi-color information as well (Baldry et al. 2010). At the longer *GALEX* wavelength, it may be harder to separate Galactic stars from low-redshift older galaxies using colors alone. As a consequence, the *GALEX* NUV count slope point in Figure 11(c) has a somewhat larger error bar at the common wavelength of ∼230 nm.

Given the above uncertainties in the *GALEX* and ERS UV galaxy count slopes, the galaxy counts show the well known trend of a steepening of the best-fit power-law slope at the bluer wavelengths, which is caused by a combination of the more significant *K*-correction *and* the shape of the galaxy redshift distribution at the selection wavelength. The galaxy count slope changes significantly from $a \gtrsim 0.44$ dex mag^{-1} at 0.23 μm wavelength to $a \simeq 0.26$ dex mag^{-1} at 1.55 μm wavelength. Hence, the galaxy counts have a slope flatter than the Euclidean value of $a \simeq 0.6$ dex mag^{-1}. However, at wavelengths below 0.4 μm the UV galaxy counts are steeper than the $a \leqslant 0.4$ dex mag^{-1} value required for their sky brightness integral to converge to a finite value, *if* they were to continue with this power-law slope for AB $\gtrsim$ 27 mag. That is, the UV galaxy counts will have to turn over with a slope flatter than $\leqslant$0.4 dex mag^{-1} for AB $\gtrsim$ 27 mag. In Section 7.3 we will confirm that they indeed do so.

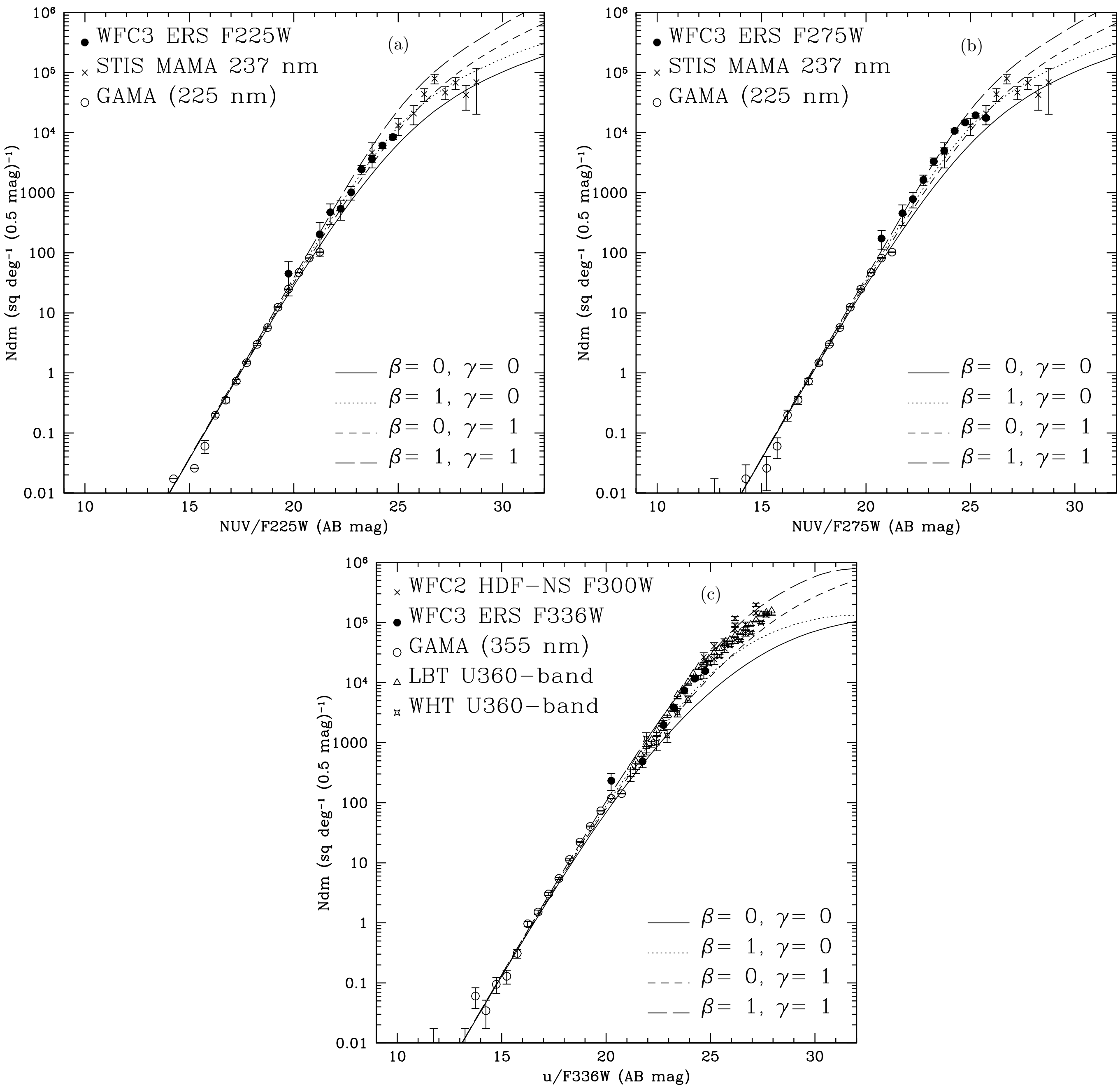

Figure 12. (a)–(c) Differential galaxy number counts for the entire flux range AB = 10–30 mag in the F225W (a), F275 (b), and F336W (c) filters. For comparison at the bright end, we added to the ERS number counts from Figure 11(a) the panchromatic GAMA survey (Driver et al. 2009) counts in NUV+$ugrizYJH$, which cover AB = 10–21 mag (Xu et al. 2005; Hill et al. 2010). At the faint end, we added the WHT U band and HDF-North and South F300W counts of Metcalfe et al. (2001), the deep LBT U-band counts of Grazian et al. (2009), as well as the deep *HST* STIS counts of Gardner et al. (2000). Best-fit luminosity and number density evolution models cover AB $\simeq$ 10–30 mag (see Driver et al. 1998; Hill et al. 2010). (d)–(g) Differential galaxy number counts for the entire flux range AB = 10–30 mag in the F435W (d), F606W (e), F775W (f), and F850LP (g) filters. Further details are given in the caption of Figures 12(a)–(c) At the faint end, we also added the HUDF counts in $BViz$ from Beckwith et al. (2006), which cover AB = 23–30 mag. (h)–(j) Differential galaxy number counts for the entire flux range AB = 10–30 mag in the F098M/F105W (h), F125W (i) and F160W (j) filters. Further details are given in the caption of Figures 12(a)–(c). At the faint end, we also added the HUDF counts from the Bouwens et al. (2010b) *YJH* data, as compiled by Yan et al. (2011b), which cover AB = 24–30 mag.

7.2. The Panchromatic Galaxy Counts for 10 mag $\lesssim$ AB $\lesssim$ 30 mag

Figures 12(a)–(j) show the galaxy number counts in the 10-band ERS images compared to a number of other panchromatic surveys at the bright end and at the faint end. At the bright end, we added the counts from the GAMA survey (Driver et al. 2009) in NUV+$ugrizYJH$, which cover AB = 10–21 mag (Xu et al. 2005; Hill et al. 2010). Details on the ground-based data obtained in the GAMA survey are given by Driver et al. (2009) and Hill et al. (2010). The GAMA survey also uses matched aperture Kron magnitudes, which are comparable to our total magnitudes used for the ERS.

The GAMA star–galaxy separation procedure is quite different than for the ERS, since there is a significant potential for contamination by stars which dominate the number counts at brighter magnitudes (Figure 11(a)). The GAMA star–galaxy separation therefore uses the ($r_{\rm PSF}$–$r_{\rm model}$) parameter to

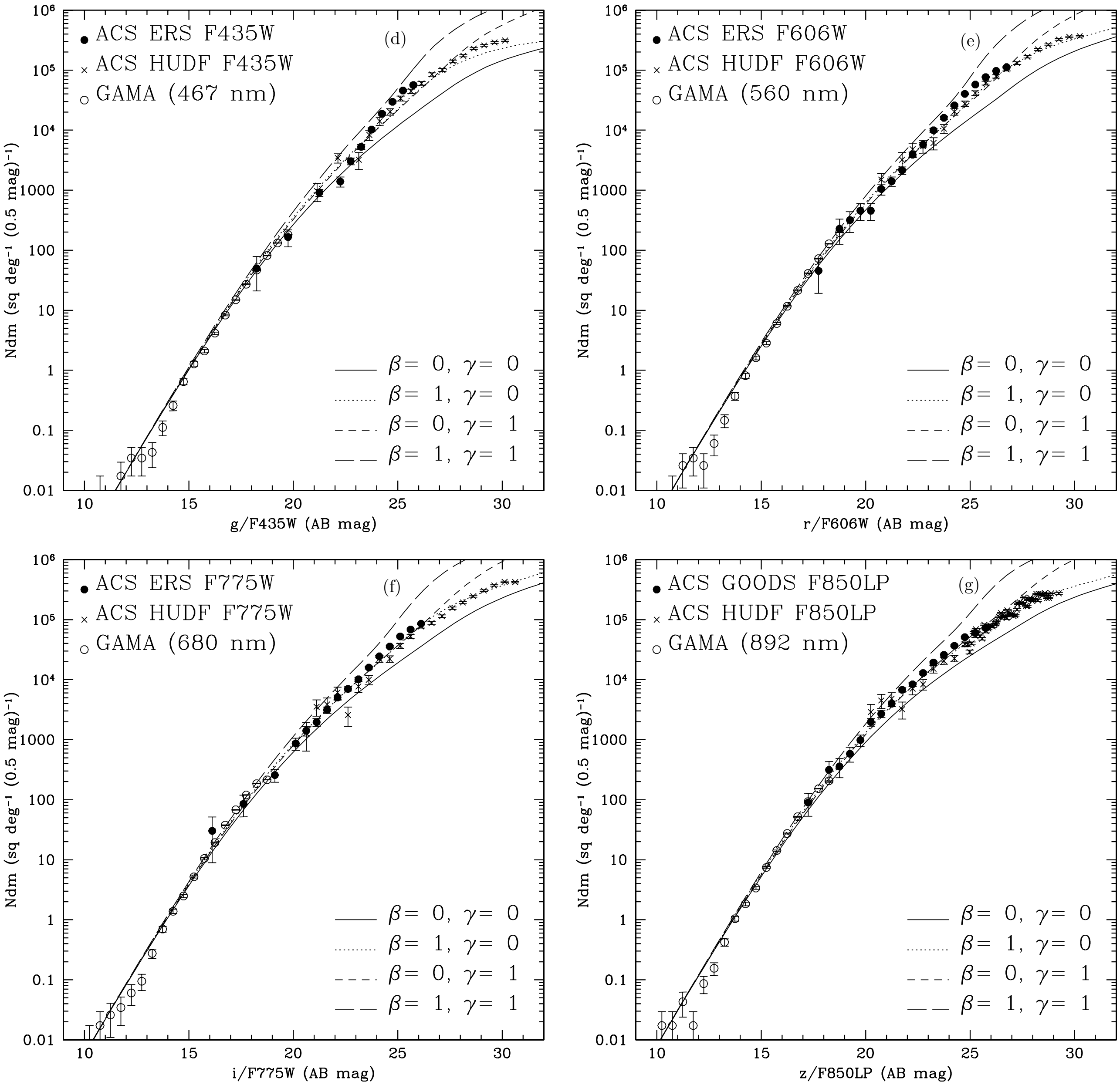

Figure 12. (Continued)

determine how extended an object is, and also uses the well-defined stellar locus in the $(g-i)$ versus $(J-K)$ color–color diagram. Details of the star–galaxy separation methods used in the GAMA survey are given by Baldry et al. (2010).

At the faint end in Figures 12(d)–(j), we added the HUDF counts in $BViz$ from Beckwith et al. (2006), which cover AB = 24–30 mag, and the HUDF counts from the Bouwens et al. (2010b) data in the F105W, F125W, and F160W filters (hereafter *YJH*), as compiled by Yan et al. (2011b), which cover AB = 24–30 mag. In the UV, we added the William Herschel Telescope (WHT) *U*-band counts and the HDF-North and South F300W counts as compiled by Metcalfe et al. (2001), the deep Large Binocular Telescope (LBT) *U*-band counts of Grazian et al. (2009), as well as the deep *HST* STIS UV counts of Gardner et al. (2000).

We note that the filter systems in the comparisons in each of Figures 12(a)–(j) are *not* quite identical, although they were chosen in every case to be as close as possible in wavelength (typically to within 0.1 dex). Hence where necessary, small but appropriate AB-mag offsets or color transformations were made between the filters and models used in each plot, following Metcalfe et al. (2001) or Windhorst et al. (1991). These corrections generally contain some color dependence. When applying them as a single AB-flux scale correction to a given survey can introduce uncertainties of order 0.1 mag in the flux scale used. Over the entire AB = 10–30 mag range shown in Figures 12(a)–(j), such ∼0.1 mag offsets would not be noticeable. However, for a detailed set of modeling in subsequent work, more subtle flux and color dependent corrections may need to be applied. This will be the subject of a future paper.

The error bars in each of the counts in Figures 12(a)–(j) are Poisson, and therefore do not include effects from cosmic variance. To increase the statistics where necessary at the bright end of each survey, bins were combined logarithmically using the local slope of the galaxy counts, following the prescription

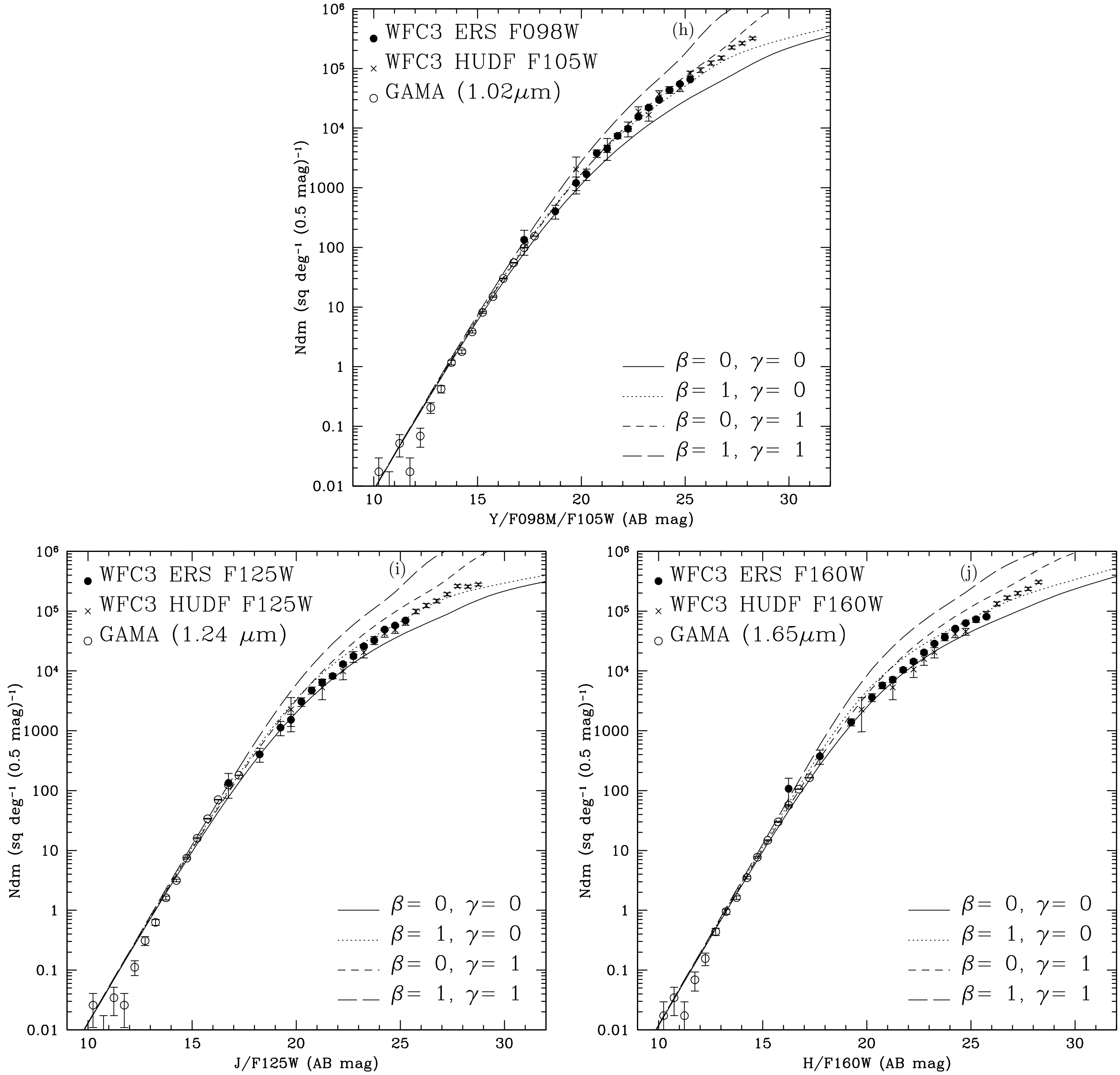

Figure 12. (Continued)

of Windhorst et al. (1984b). At the faint end, the counts are not plotted in Figures 12(a)–(j) fainter than the flux level where these are deemed complete. Based on Figures 9 and 11(a), this occurs in general where the counts turn over significantly within the statistical error bars. Hence, in principle, the panchromatic counts of Figures 12(a)–(j) should be comparable over the entire flux range AB $\simeq$ 10–30 mag, except for the effects of cosmic variance. The latter is small for the panchromatic $\sim$116 deg^2 GAMA survey, but it could be important for the other panchromatic survey areas plotted, such as the ERS and the HUDF which are both (disjoint) parts of GOODS-S, as well as the HDF-North (in GOODS-North) plus the HDF-South and various other ground-based surveys in the U band.

In the flux range where the panchromatic GAMA and HUDF counts in Figures 12(a)–(j) overlap with the panchromatic ERS counts, the agreement is in general quite good, except at the bright end of the ERS, which suffers from cosmic variance, and from the fact that the GOODS/ERS field was chosen to be devoid of objects much brighter than AB = 18 mag. As a consequence, the bright end of the ERS galaxy counts also suffers somewhat from incompleteness. The same is true for the bright end of the HUDF, which suffers similarly from cosmic variance and the avoidance of objects much brighter than AB $\sim$ 21–22 mag when that field was selected in early 2003 for the ultradeep *HST* survey. The HUDF is adjacent to, but does not overlap with the ERS area (see Figure 3). The HUDF galaxy counts in $BVizY_sJH$ are in good agreement with the ERS galaxy counts to the flux levels where the panchromatic ERS counts are considered complete (AB $\simeq$ 26–27 mag in Figure 11(a)).

The good agreement between these various surveys also implies that the flux scales of the panchromatic ERS counts are approximately correct. Had one of the ERS filter zero points been off significantly (e.g., by more than 0.1–0.2 mag), we would have noticed this as a significant offset between the counts. Note this argument only holds for the counts at AB $\gtrsim$ 20 mag, as these cover the same general area of sky in the GOODS-South field. Hence, cosmic variance likely affects these counts similarly over such scales ($\lesssim$ 30%; Somerville et al. 2004).

7.3. Modeling the Panchromatic Galaxy Counts for 10 mag $\lesssim$ AB $\lesssim$ 30 mag

Figures 12(a)–(j) overplot simple galaxy evolution models by Driver et al. (1995, 1998), which have been updated for the current comparison with the ERS. Driver et al. (1995, 1998) and Cohen et al. (2003) provide further details of these models. In short, they use the best available local LF as a function of galaxy type, and *K*-corrections from the Bruzual & Charlot (2003) spectral evolution models, also as a function of galaxy type. The local galaxy LF then gets integrated with the *WMAP* year 7 (Komatsu et al. 2011) cosmological volume element to predict the number density of galaxies observed to the total-flux limit in each ERS filter. These models also include internal reddening as a function of galaxy type.

These models have been updated with the best available local panchromatic LFs in *ugrizYJHK* from the Millennium Galaxy Catalog survey by Hill et al. (2011), and in the UV they use the *GALEX* LFs of Robotham & Driver (2011). These LFs will be updated in future work with GAMA redshifts from the three-year Anglo-Australian Telescope survey that was concluded in 2010. Robotham et al. (2010) provide further details on the GAMA redshift survey. This GAMA data set is currently 99% redshift complete for $r_{\rm Petro} \simeq$ 19.4 mag, and provides high-fidelity, matched-volume panchromatic LFs, which are essential to interpret the higher-redshift panchromatic ERS work.

Evolution of the faint-end LF slope is not yet included in these simple models, but the panchromatic local GAMA LFs automatically includes the well-known steepening of the local LF toward shorter rest-frame wavelengths, where the local LF is dominated by the more rapidly star-forming late-type galaxies (see Driver et al. 1998; Robotham & Driver 2011; Hill et al. 2011). The epoch-dependent galaxy redshift distribution is also *not* an input to these models, but can instead be inferred from the local LF as a function of type (e.g., Driver et al. 1996), the total constraints provided by the panchromatic galaxy counts (Figures 12(a)–(j)), the adopted *K*-corrections as a function of galaxy type, and the adopted evolutionary model parameters. These simple evolution models used are either a pure luminosity evolution (PLE) model with $e(z) = 2.5 \log[(1+z)^{\beta}]$ and PLE exponent β, *or* a number density evolution (NDE) model with $n(z) = n_o\,[(1+z)^{\gamma}]$ and NDE exponent γ, or a combination thereof.

Based on the currently available, best panchromatic local GAMA LFs, Figures 12(a)–(j) show for AB = 10–30 mag the PLE model prediction with PLE exponent $\beta = 1$ (dotted lines), the NDE model prediction with NDE exponent $\gamma = 1$ (short-dashed lines), *or* a combination of both models indicated by *both* parameters $\beta = \gamma = 1$ (long-dashed lines). The solid lines show in all cases the non-evolving model ($\beta = \gamma = 0$).

Over the entire flux range AB $\simeq$ 10–30 mag, Figures 12(a)–(j) show that no single PLE model fits all the available galaxy count data, since there is not enough volume at high redshift to make any PLE model fit the high observed counts, especially in the visual to near-IR (Figures 12(d)–(j)). This means that one has to invoke NDE as well, i.e., $\beta \gtrsim 1$ and some modest amount of luminosity evolution for $\gamma \gtrsim 0$. The best models using these PLE or pure density evolution (PDE) prescriptions are either the $\beta \simeq 1$ or the $\gamma \simeq 1$ model. Figures 12(a)–(j) also shows that no single combined PLE+NDE model fits the panchromatic galaxy counts in all 10 bands simultaneously over the entire observed range AB $\simeq$ 10–30 mag, not even with the best available panchromatic local LF from the GAMA survey (Hill et al. 2011).

In particular, Figures 12(d)–(j) show that at the faint end of the galaxy counts in *YJH* there exists a significant excess in observed object numbers compared to these simple models. This could be due to either an additional population of objects at high redshifts, or—more likely—due to lower luminosity objects at lower redshifts, and/or because some essential aspects are missing in these models. A detailed discussion of these possibilities is beyond the scope of the current paper, but the reader is referred to, e.g., Bouwens et al. (2010b), Yan et al. (2011b), and Wyithe et al. (2011) for a discussion of some of these possibilities.

More realistic galaxy evolution models would be ones in which the faint-end Schechter LF-slope α *also* evolves with redshift, as has been suggested by, e.g., Ryan et al. (2007) and Khochfar et al. (2007). In particular, the faint-end LF-slope α steepens significantly at higher redshifts, which was suggested by, e.g., Yan & Windhorst (2004), Ryan et al. (2007), Hathi et al. (2010), and Oesch et al. (2010b). One would like to compare our panchromatic ERS galaxy counts from 0.2 to 2 μm over the entire observed range AB = 10–30 mag (Figures 12(a)–(j)) to state-of-the-art hierarchical simulations that reach from $z = 8$ to $z = 0$, and properly fold star formation and stellar population evolution models with these ΛCDM simulations. Such models have been made, e.g., by Croton et al. (2006), de Lucia & Blaizot (2007), and Nagamine et al. (2005a, 2005b), and are discussed in further detail by, e.g., Kitzbichler & White (2007), Monaco et al. (2007), and Nagamine (2006). It is difficult for such models to predict reliable panchromatic galaxy counts from 0.2 to 2 μm that cover the entire observed range AB = 10–30 mag, because such simulations take a very large amount of computing time to cover the low-redshift regime ($z \lesssim 3$), to cover the entire galaxy LF, and to let and them run all the way to $z = 0$. In addition, such models need to include increasingly complex physics with cosmic time, such as hierarchical merging and/or downsizing, feedback processes from SNe and AGNs, and how these processes changed the faint end and bright end of the galaxy LF, respectively, over cosmic time, as well as include the physics of dust. This will be the subject of a future paper that compares the observed panchromatic galaxy counts from 0.2 to 2 μm over the entire flux range AB = 10–30 mag to available hierarchical models.

For now, we conclude that the simple PLE+PDE models with the best available observed panchromatic local LF from GAMA can explain each of the 10-band counts for 10 mag $\lesssim$ AB $\lesssim$ 30 mag *individually*, but no single one of the simple PLE+NDE models can explain the counts over this entire flux range in all 10 filters *simultaneously*.

8. SUMMARY AND CONCLUSIONS

In this paper, we presented the new *HST* WFC3 ERS observations in the GOODS-South field. We presented the scientific rationale of this ERS survey and its data, the data taking plus data reduction procedures of the panchromatic 10-band ERS mosaics. We described in detail the procedure of generating object catalogs across the 10 different ERS filters.

The new WFC3 ERS data provide calibrated, drizzled mosaics in the UV filters F225W, F275W, and F336W, as well as in the near-IR filters F098M (Y_s), F125W (J), and F160W (H) in 1–2 *HST* orbits per filter. Together with the existing *HST* Advanced Camera for Surveys (ACS) GOODS-South mosaics in the $BViz$ filters, these panchromatic 10-band ERS data cover 40–50 arcmin^2 at 0.″07–0.″15 FWHM resolution and 0.″090 Multidrizzled pixels to depths of AB $\simeq$ 26.0–27.0 mag (5σ) for point sources and AB $\simeq$ 25.5–26.5 mag for compact galaxies. The galaxy samples are $\gtrsim$50% complete to these limits, and $\gtrsim$99.97% reliable.

We also described the high quality star–galaxy separation made possible by the superb resolution of *HST*/WFC3 and ACS over a factor of 10 in wavelength to AB $\simeq$ 25–26 mag from the UV to the near-IR, respectively, using proper motion and $BViz$ colors to confirm the star–galaxy separation procedure, which has an overall reliability of $\gtrsim$87% for stars. Our main science results are as follows.

1. We present the resulting Galactic star counts and galaxy counts in 10 different filters. From the ERS data, these could be accurately determined from AB $\simeq$ 19 mag to AB $\simeq$ 26 mag over a full factor of 10 in wavelength from the mid-UV to the near-IR.
2. Both the Galactic star counts and the galaxy counts show mild but significant trends of decreasing count slopes from the mid-UV to the near-IR over a factor of 10 in wavelength.
    a) The faint end of the Galactic star count slope is remarkably flat at all wavelengths from the Balmer break to the near-IR. The values of the best-fit power-law star count slope is in general of order 0.03–0.05 dex mag^{-1} above the Balmer break, i.e., well below Euclidean value of 0.6 dex mag^{-1}. This shows that to a depth of AB $\simeq$ 25–26 mag at all wavelengths in the range 0.2–2 μm, the ERS images are looking through most of the thick stellar disk of our Galaxy at intermediate latitudes.
    b) We measured the proper motion for 103 ERS stars, most of which have colors consistent with the stellar locus in a $(i - z)$ versus $(B - V)$ color–color diagram. Their ensemble *average* proper motion is $\sim$3.06 $\pm$ 0.67 mas year^{-1}. This is a 4.6σ measurement of the average proper motion of faint stars with 16 mag $\lesssim$ AB $\lesssim$ 26 mag. At the typical distance of these faint Galactic K–M type stars ($\sim$10 kpc), the average ERS proper motion correspond to a velocity of $\sim$145 km s^{-1}, consistent with Galactic structure models and previous stellar radial velocity and proper motion observations at much brighter levels.
3. The galaxy count slope changes significantly from $a \simeq 0.44$ dex mag^{-1} at 0.23 μm wavelength to $a \simeq$ 0.26 dex mag^{-1} at 1.55 μm wavelength, showing the well known trend of a steepening of the best-fit power-law slope at the bluer wavelengths. This is caused by a combination of the more significant K-correction and the shape of the galaxy redshift distribution at the selection wavelength.
4. We combine the 10-band ERS counts with the panchromatic GAMA counts at the bright end (10 mag $\lesssim$ AB $\lesssim$ 20 mag), and with the ultradeep HUDF counts in $BVizY_sJH$ and other available *HST* UV counts at the faint end (24 mag $\lesssim$ AB $\lesssim$ 30 mag). The galaxy counts are now well measured over the entire flux range 10 mag $\lesssim$ AB $\lesssim$ 30 mag over nearly a factor of 10 in wavelength.
5. We fit simple galaxy evolution models to these panchromatic galaxy counts over this entire flux range 10 mag $\lesssim$ AB $\lesssim$ 30 mag, using the best available 10-band local galaxy LFs from the GAMA survey (Hill et al. 2010), as well as simple prescriptions of luminosity and/or density evolution. While these models can explain each of the 10-band counts for 10 mag $\lesssim$ AB $\lesssim$ 30 mag individually, no single one of the simple PLE+NDE models can explain the counts over this entire flux range in all 10 filters simultaneously. Any more sophisticated models of galaxy assembly, including hierarchical merging and/or downsizing with or without feedback, need to at least reproduce the overall constraints provided by the current panchromatic galaxy counts for 10 mag $\lesssim$ AB $\lesssim$ 30 mag over a factor of 10 in wavelength.
   These surveys also emphasize the need for extending this work to levels fainter than AB $\gtrsim$ 30 mag and at longer wavelengths, which the *JWST* will do for wavelengths in the range 0.6–28 μm after its launch after 2015. The unique abilities of WFC3 to do deep UV imaging will need to be explored fully before that time.
6. We show examples of interesting panchromatic faint galaxy structure in intermediate-redshift objects, including early-type galaxies with nuclear star-forming rings and bars, and/or weak AGN activity, and some objects of other unusual appearance.

The panchromatic ERS database is very rich in structural information at all rest-frame wavelengths where young or older stars shine during the peak epoch in the cosmic star formation rate ($z \simeq$ 1–2) and constitutes a unique new *HST* data base for the community to explore in the future.

This paper is based on Early Release Science observations made by the WFC3 Scientific Oversight Committee. We are grateful to the Director of the Space Telescope Science Institute, Dr. Matt Mountain, for generously awarding Director's Discretionary time for this program. We thank Drs. Neill Reid, Ken Sembach, Ms. Tricia Royle, and the STScI OPUS staff for making it possible to have the ERS data optimally scheduled. We also thank WFC3 IPT and the GSFC WFC3 Project for their very hard dedicated work since 1998 to make this wonderful instrument work, and for their timely delivery of the essential hardware and software to make the acquisition and reduction of the new WFC3 data possible. We also thank the entire GOODS team and in particular Drs. Norman Grogin and Mauro Giavalisco for making the exquisite GOODS v2.0 mosaics available. We thank Drs. Norman Grogin and Paul Schmidtke for helpful discussions. We thank the referee for very thoughtful suggestions, which helped improve the presentation of this paper, and for prompting a more detailed study of the ERS stellar proper motions and colors, which we believe illustrates the multi-faceted promise of the ERS data.

Support for *HST* program 11359 was provided by NASA through grant GO-11359 from the Space Telescope Science Institute, which is operated by the Association of Universities for Research in Astronomy, Inc., under NASA contract NAS 5-26555. R.A.W. also acknowledges support from NASA *JWST* Interdisciplinary Scientist grant NAG5-12460 from GSFC. H.Y. is supported by the long-term fellowship program of the Center for Cosmology and AstroParticle Physics (CCAPP) at The Ohio State University.

We thank the STS-125 astronauts for risking their lives during the Shuttle Servicing Missions SM4 to Hubble, and for successfully installing WFC3 into *HST* in 2009 May. We dedicate this paper to the memory of the STS-107 Columbia Shuttle astronauts and of Dr. Rodger Doxsey, who during their lives contributed so much to the Space Shuttle and the *Hubble Space Telescope* projects.

APPENDIX A

THE WAVELENGTH-DEPENDENT UVIS GEOMETRIC DISTORTION CORRECTION

Given the issues related to the GDC discussed in Section 4.2.2, it was apparent that some astrometric residuals remained—at the level of $\lesssim$2–3 Multidrizzled pixels—that were a function of position across both UVIS detectors, after the shifts and rotations had been removed. A worst case is shown in the lower panel of Figure 4(a). These residuals were apparent between the three UVIS filters, as well as relative to the GOODS astrometric frame. At the time of the data reduction, the best available Instrument Distortion Coefficients (IDCtab's; file t982101i_uv_idc.fits)—which are used for the GDC—had been created using the WFC3 SMOV *F*606*W* data *alone*[30]. This GDC did *not yet* include any wavelength-dependent distortion terms, though these will be measured during Cycle 18 or beyond[31], and distributed to the community by the WFC3 instrument team. Since our WFC3/UVIS data are all taken at wavelengths below 3500 Å, it is likely that the remaining astrometric residuals are indicative of the absence of these color-dependent terms in the currently existing GDC tables. The wavelength-dependent terms of the GDC come from the different index of refraction of the glass optics and filters in the UVIS channel of WFC3. This is in addition to the first- to third-order geometric distortion coefficients, which results from the CCD tilt (which was necessary to minimize internal reflections), and from other reflective optics, and are therefore largely wavelength-independent.

The ultimate goal of the UVIS part of the WFC3/ERS is to create images in F225W, F275W, and F336W filters at the same pixel scale (0$''$.030 per pixel) and astrometric grid as the GOODS ACS images (Giavalisco et al. 2004) of the same portion of the GOODS-South field. As discussed in Section 2, the eight ERS UVIS pointings were designed to overlap with each other, in order to achieve the best possible astrometric precision. After the extensive astrometric work described above, it turned out that we had reached the limit of what was possible with the present *wavelength-independent* geometric distortion solution. We were able to align all UVIS images such that the *average* object was well aligned with the GOODS *B*-band image. However, objects near the individual UVIS field edges were not well aligned (lower panel of Figure 4(a)). Figure B.1 of the WFC3 Instrument Handbook (Wong et al. 2010) also suggests that in these locations the geometric distortion is the largest. This was most noticeable on the few stars in the overlap regions between pointings, as Figure 4(a) demonstrated.

Some of these stars also showed significant proper motion between the original 2004–2007 GOODS observations and the 2009 ERS observations, complicating their use as astrometric fiducials (see Sections 4.3.2 and 6). This is quite visible as significant color offsets in some of the ERS bright star images in the very high resolution versions of Figures 5(a) and (b) and 6(c), which are available at the URL given in the figure caption. In attempting to create a 0$''$.030 per pixel UVIS mosaic, the stars in the overlap regions of the eight UVIS pointings were somewhat elongated (Figure 4(a)), even though the exposures from the same UVIS orbit were well aligned—i.e., having round stars and astrometric residuals to a fraction of a pixel—*and* even though each pointing was well matched to the GOODS frame. In other words, even after correcting the WCS in the FITS headers for *both* the relative *and* the absolute position deviations, there still remained some astrometric residuals primarily at the field edges, that we suspect are likely due to the uncertain wavelength dependence of the GDC (Figure 4(b)).

Figure 4(b) shows the astrometric residuals for four of our ERS pointings in the F336W filter (visits 25, 26, 29, and 30). Each frame within a visit was registered using the MultiDrizzle scripts of Koekemoer et al. (2002), which CR-cleaned and cross-correlated the images, to revise the flat-fielded (FLT) image WCS header keywords, as described in Section 4.2.1. These images were then drizzled with PIXFRAC = 1.0 to a scale of 0$''$.030 per pixel and to a position angle of 0 deg (final_rot = 0). The PA(V3) was 111 deg. Catalogs were then created with SExtractor (Bertin & Arnouts 1996), which were in turn matched in equatorial coordinates to a similar catalog made from the GOODS-South *B*-band image (GOODS v2.0; Giavalisco et al. 2004; N. Grogin 2009, private communication). Note that *all four* visits in Figure 4(b) show similar bimodal residuals, suggesting that this is a systematic error. We suspect that this is due to the *wavelength-dependent* geometric distortion in the UV, since the only distortion solution available at the time of the data processing was measured in the F606W filter. Since two distinct blobs of points occur in similar locations in all four panels of Figure 4(b), the MultiDrizzle images of objects seen in *only one* pointing—which includes 80%–90% of the total ERS area (see Figures 3 and 8(a))—*are* round at 0$''$.090 pixel sampling. However, the images of the brighter objects in the overlap areas between mosaic pointings—10%–20% of the total area—are not always completely round, as shown in Figure 4(a). (Visual inspection of the F225W and F275W mosaics showed similar trends for bright stars as seen for F336W in Figures 4(a) and (b)—confirming our conjecture that this is due to the GDC only having been calibrated in the F606W filter. However, these trends are seen at lower S/N than in F336W—since faint stars are red, see Section 4.3.2 and figures therein—and so Figures 4(a) and (b) are not reproduced here for F225W and F275W.)

When Multidrizzling the four exposures of each pointing, each individual object is well aligned with itself. However, in the WFC3 field corners, an object can be offset from the GOODS WCS by ±0$''$.1–0$''$.2 (Figures 4(a) and (b)). In the area of field overlap, an object in the ERS image corners or at a visit's field edges can thus be misaligned with itself by ∼0$''$.1–0$''$.2, and so be elongated (see Figure 4(a)), but still be *on average* on top of the GOODS v2.0 WCS. In other words, with the *current* wavelength-independent GDC and MultiDrizzle, we cannot have it both ways for a given object in the image borders of the ERS mosaic, until the wavelength-dependent GDC has been fully measured in the UV, *and* a sufficient larger number of dither points is available to take full advantage of the full 0$''$.0.0395 pixel sampling of the WFC3 UVIS images. This is at the moment not the case. Therefore, in this paper we use the total-flux measurements from the UVIS images that were Multidrizzled at 0$''$.090 pixel^{-1}, and use large enough apertures that the total flux measurements are reliable.

[30] http://www.stsci.edu/hst/wfc3/idctab_lbn

[31] http://www.stsci.edu/hst/wfc3documents/newsletters/STAN_09_01_2009

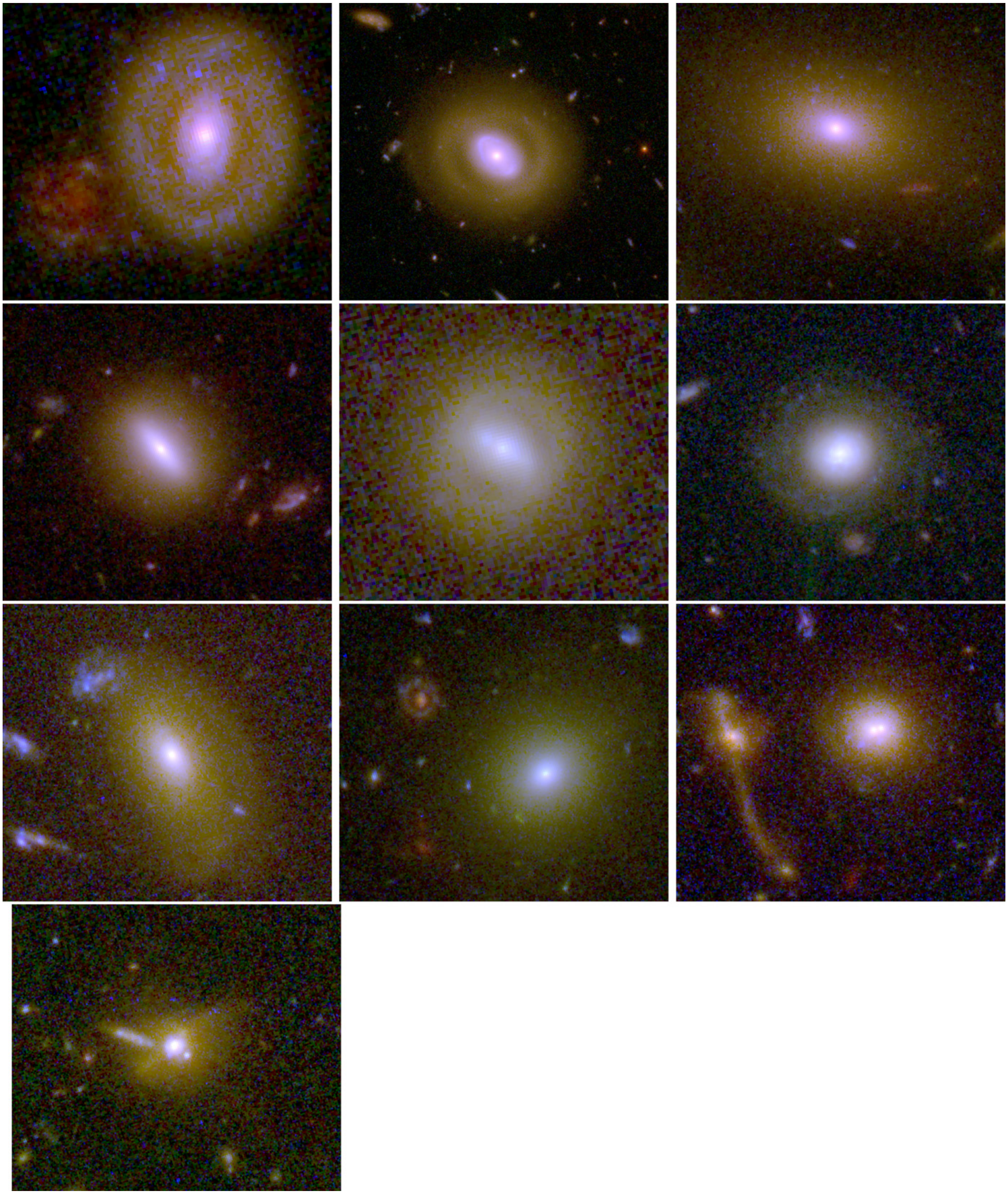

Figure 13. Panchromatic postage stamps of early-type galaxies in the ERS with nuclear star-forming rings, bars, or other interesting nuclear structure. Each postage stamp is displayed at a slightly different color stretch that best brings out the UV nuclear structure. For further details, see Rutkowski et al. (2011).

For the WFC3 IR Channel, the GDC has only been measured in the F160W filter[32], and so the GDC in the other two ERS IR filters F098M and F125W is correspondingly more uncertain. However, because the WFC3 IR Channel GDC is much smaller to begin with (see Wong et al. 2010)—due to the IR Channel design—and because of the larger IR channel pixels, the wavelength dependence of the IR Channel GDC is much less of an issue than for the WFC3 UVIS channel. As for

[32] http://www.stsci.edu/hst/wfc3documents/newsletters/STAN_09_01_2009

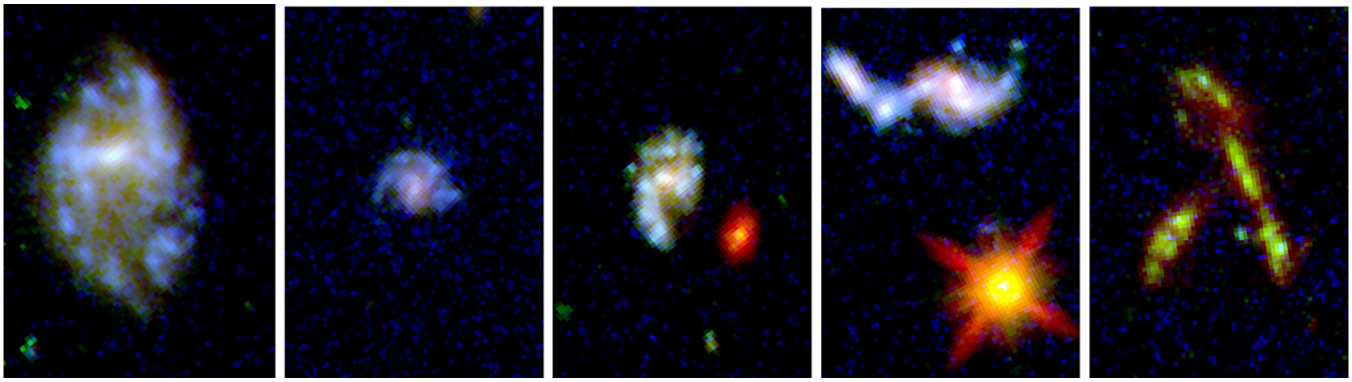

Figure 14. Panchromatic postage stamps of objects with interesting morphological structure in the 10-band ERS color images of the GOODS-South field: from left to right, high signal-to-noise detections of ERS galaxies resembling the main cosmological parameters H_0, Ω, ρ_o, w, and Λ, respectively. These images illustrate the rich and unique morphological information available in the 10-band panchromatic ERS data set.

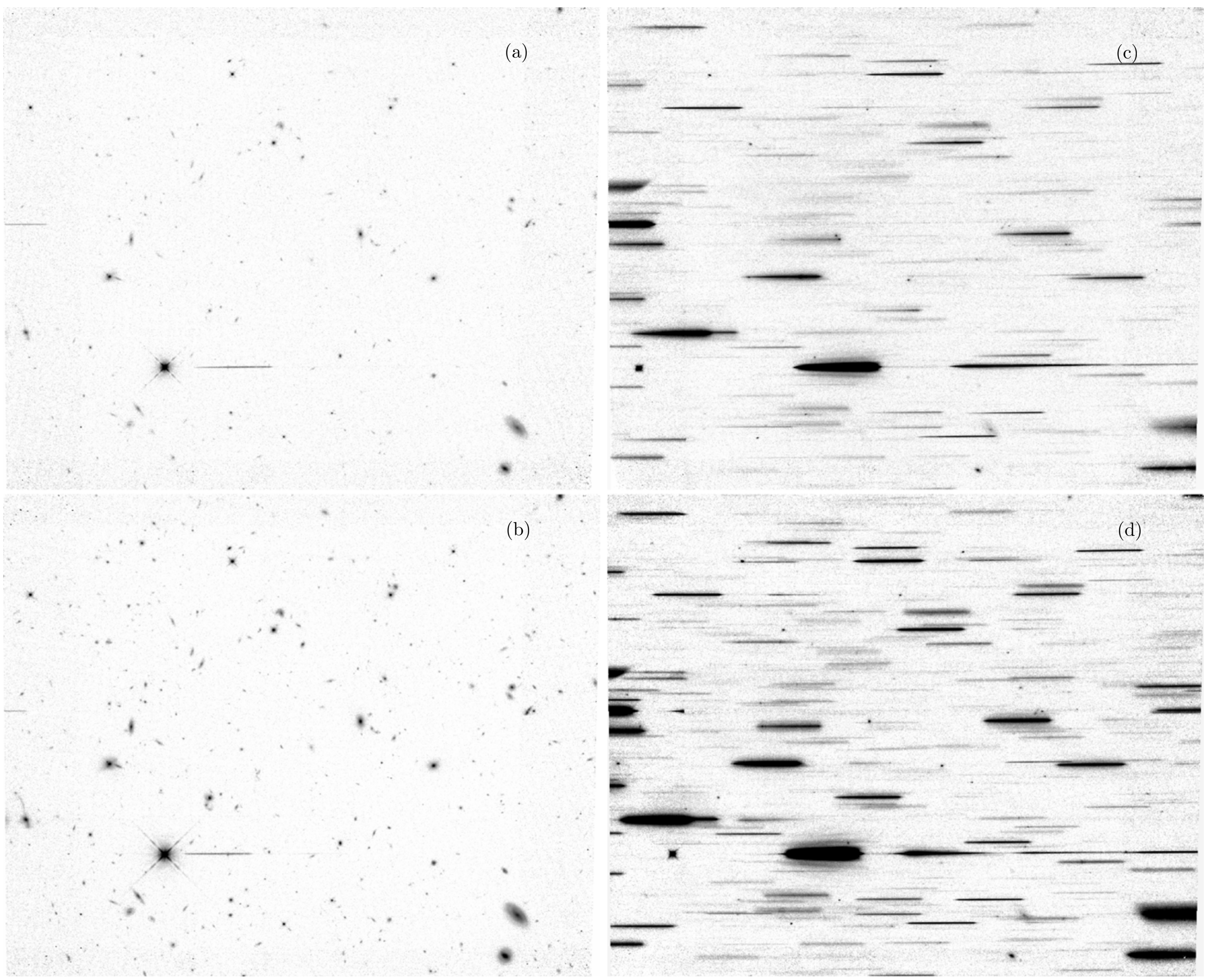

Figure 15. (a)–(d) 4212 s WFC3 G102 (top right) and G141 (bottom right) grism exposures of a single WFC3 pointing in the GOODS-South field (green box in Figure 3), together with their 1612 s finder images in F098M (top left) and G141 (bottom left), respectively. Each image is a 4-point dithered mosaic. (For best display, please zoom in on the full-resolution PDF version of this image.) All brighter object grism spectra show a zeroth-order image to their left, displaced by about twice the spectral image length, which should not be confused with real emission lines. Many faint object spectra are visible to a continuum flux of AB $\lesssim$ 25–25.5 mag, including many faint emission line galaxies. For details, see Straughn et al. (2009, 2011). (e) and (f) Examples of WFC3 G102 and G141 spectra of emission line galaxies extracted from the ERS grism images ((a)–(d)). The left panel shows an emission line galaxy at $z = 0.738$ and the right panel at $z = 0.610$. The latter also shows the available lower-resolution ACS G800L grism spectrum (green). The WFC3 G102 and G141 spectra allow for low-resolution faint object spectroscopy over the entire 0.80–1.70 μm range unimpeded by the ground-based OH-forest. For further details, see Straughn et al. (2009, 2011).

(A color version of this figure is available in the online journal.)

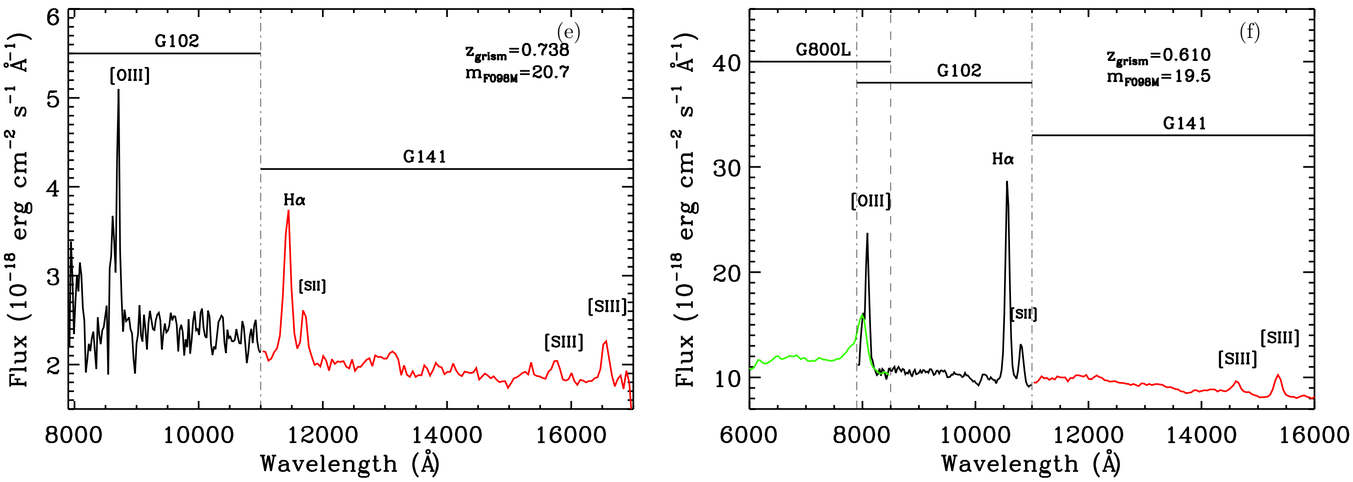

Figure 15. (Continued)

the WFC3 UVIS channel, the wavelength dependence of the IR Channel GDC will be measured in more detail in Cycle 17 and beyond, and will be applied to a future version of the ERS data release and discussed in subsequent ERS papers.

APPENDIX B

OTHER APPLICATIONS OF THE ERS DATA

B.1. Interesting Classes of Objects in the Panchromatic ERS Mosaics

Figure 13 shows several panchromatic postage stamps of lower-redshift early-type galaxies in the ERS with nuclear star-forming rings, bars, or other interesting nuclear structure. Each postage stamp is displayed at a slightly different color stretch, that best brings out the UV nuclear structure. Rutkowski et al. (2011) present examples of ellipticals at $z \simeq 0.3$–1.5 with various amounts of UV-excess flux. These galaxies are red and relatively featureless in the optical, but show considerable emission in the UV, which is not all point-like. Hathi et al. (2010) and Ryan et al. (2011) present ERS samples of faint UV-dropouts and very high redshift red galaxies, respectively. Many more such studies can be done with the ERS data.

Figure 14 shows panchromatic postage stamps of objects with interesting morphological structure in the 10-band ERS color images of the GOODS-South field, yielding high-S/N detections of galaxies resembling the main cosmological parameters H_0, Ω, ρ_o, w, and Λ, respectively. The panchromatic galaxy morphology and structure in the ERS images is so rich that a patient investigator can find galaxies of nearly any appearance in the epoch $z \simeq 1$–3. This is because galaxy merging was in full swing in this epoch.

B.2. Examples of Uses and Future Potential of WFC3 IR Grism Data

Figures 15(a)–(d) display the WFC3 G102 and G141 grism images of the same region in the GOODS-South field (green box in Figure 3), together with short finder exposures in the WFC3 grism continuum filters F098M and F140W. For a detailed discussion of the ACS G800L and WFC ERS G102 and G141 grism spectra, please see Straughn et al. (2009, 2011). All brighter object WFC3 grism spectra in Figures 15(a)–(d) show a zeroth-order image to their left, displaced by about twice the spectral image length, which should not be confused with real emission lines. When one zooms in on the full-resolution version of this image (see the caption of Figures 15(a)–(d)), many faint object spectra are visible to a continuum flux as faint as AB $\sim$ 25–25.5 mag in two *HST* orbits, including many faint emission line galaxies.

Figures 15(e) and (f) show examples of some specific WFC3 G102 and G141 spectra for emission line galaxies in the ERS at $z = 0.738$ and $z = 0.610$. For the emission line galaxy at $z = 0.610$, the available lower-resolution ACS G800L grism spectrum is also shown in green. For further details, see Straughn et al. (2011). Figure 15(f) shows that WFC3 near-IR grisms G102 and G141 have a spectral resolution of $R \simeq 210$ and $R \simeq 130$, respectively, while the ACS G800L has a lower resolution of $R \simeq 100$. It is clear from Figure 15(f) that $R \gtrsim 200$ is far superior for faint emission-line (and by implication also for weak absorption feature) detection than an $R \sim 100$ grism. This should be a critical consideration for the design of the JDEM/WFIRST missions that are now being planned (Blandford et al. 2010) to carry out wide-field near-infrared imaging and grism spectroscopy from space for this coming decade.

In conclusion, the WFC3 broadband IR filters and its G102 and G141 grisms provide low-resolution imaging and faint object spectroscopy over the entire 0.80–1.70 μm range, unimpeded by the ground-based OH forest. They have shown the tremendous power of the WFC3 IR grism data above Earth's atmosphere, which are now used by a number of different WFC3 GO programs in *HST* Cycle 17 and beyond. They also illustrate the discovery power of the new frontier that will be opened up by the near- to mid-infrared 6.5 m *JWST* after its launch in 2015 (Gardner et al. 2006; Windhorst et al. 2006), and by future wide-field near-infrared space missions such as *JDEM*/*WFIRST* and Euclid.

REFERENCES

Abraham, R. G., Ellis, R. S., Fabian, A. C., Tanvir, N. R., & Glazebrook, K. 1999, MNRAS, 303, 641

Abraham, R. G., Tanvir, N. R., Santiago, B. X., Ellis, R. S., Glazebrook, K., & van den Bergh, S. 1996, MNRAS, 279, L47

Abraham, R., et al. 2007, ApJ, 669, 184

Afonso, J., Mobasher, B., Koekemoer, A., Norris, R. P., & Cram, L. 2006, AJ, 131, 1216

Anderson, J. 2002, in The 2002 HST Calibration Workshop, ed. S. Arribas, A. Koekemoer, & B. Whitmore (Baltimore, MD: STScI), 13

Anderson, J. 2003, in ASP Conf. Ser. 296, ed. G. Piotto, G. Meylan, S. G. Djorgovski, & M. Riello (San Francisco, CA: ASP), 125
Anderson, J. 2007, Instrument Science Report ACS 2007-08 (Baltimore, MD: STScI)
Baggett, S., Boucarut, R., Telfer, R., Kim Quijano, J., & Quijada, M. 2007, Instrument Science Report WFC3 2007-03 (Baltimore, MD: STScI)
Baldry, I. K., et al. 2010, MNRAS, 404, 86
Balestra, I., et al. 2010, A&A, 512, 12
Battaglia, G., et al. 2005, MNRAS, 364, 433
Beckwith, S. V., et al. 2006, AJ, 132, 1729
Bertin, E., & Arnouts, S. 1996, A&AS, 117, 393
Blandford, R. D., et al. (ed.) 2010, in New Worlds, New Horizons in Astronomy and Astrophysics, Committee for a Decadal Survey of Astronomy and Astrophysics National Research Council (Washington, DC: The National Academies Press), http://www.nap.edu/catalog/12951.html
Bond, H. E., & Kim Quijano, J. (ed.) 2007, Wide Field Camera 3 Instrument Handbook, Version 1.0 (Baltimore, MD: STScI)
Bouwens, R. J., et al. 2010a, ApJ, 708, L69
Bouwens, R. J., et al. 2010b, ApJ, 709, L133
Bruzual, G., & Charlot, S. 2003, MNRAS, 344, 1000
Burgarella, D., et al. 2006, A&A, 450, 69
Clarkson, W., et al. 2008, ApJ, 684, 1110
Cohen, S. H., Windhorst, R. A., Odewahn, S. C., Chiarenza, C. A. T., & Driver, S. P. 2003, AJ, 125, 1762
Cohen, S. H., et al. 2006, ApJ, 639, 731
Cohen, S. H., et al. 2011, BAAS, 43, 2011
Comastri, A., et al. 2011, A&A, 526, L9
Conselice, C. J., Bershady, M. A., Dickinson, M., & Papovich, C. 2003, AJ, 126, 1183
Croton, D. J., et al. 2006, MNRAS, 365, 11
de Lucia, G., & Blaizot, J. 2007, MNRAS, 375, 2
de Lucia, G., Springel, V., White, S. D. M., Croton, D., & Kauffmann, G. 2006, MNRAS, 366, 499
di Matteo, T., Springel, V., & Hernquist, L. 2005, Nature, 433, 604
Dickinson, M., Papovich, C., Ferguson, H. C., & Budavari, T. 2003, ApJ, 587, 25
Dickinson, M., et al. 2004, ApJ, 600, L99
Driver, S. P., Couch, W. J., Phillipps, S., & Windhorst, R. A. 1996, ApJ, 466, L5
Driver, S. P., Fernandez-Soto, A., Couch, W. J., Odewahn, S. C., Windhorst, R. A., Phillipps, S., Lanzetta, K., & Yahil, A. 1998, ApJ, 496, L93
Driver, S. P., Windhorst, R. A., Ostrander, E. J., Keel, W. C., Griffiths, R. E., & Ratnatunga, K. U. 1995, ApJ, 449, L23
Driver, S. P., et al. 2009, Astron. Geophys., 50, 5.12
Ferreras, I., et al. 2009, ApJ, 706, 158
Finkelstein, S., et al. 2011, ApJ, submitted (arXiv:1008.0634)
Gardner, J. P., Brown, T. M., & Ferguson, H. C. 2000, ApJ, 542, L79
Gardner, J. P., et al. 2006, Space Sci. Rev., 123, 485
Giacconi, R., et al. 2002, ApJS, 139, 369
Giavalisco, M., et al. 2004, ApJ, 600, L93
Glazebrook, K., Ellis, R., Santiago, B., & Griffiths, R. 1995, MNRAS, 275, L19
Grazian, A., et al. 2009, A&A, 505, 1041
Grogin, N., et al. 2009, GOODS v2.0 mosaics, http://archive.stsci.edu/pub/hlsp/goods/v2/h_goods_v2.0_rdm.html
Gruppioni, C., et al. 2010, A&A, 518, L27
Haardt, F., & Madau, P. 1996, ApJ, 461, 20
Harris, H. C., et al. 2006, AJ, 131, 571
Hartig, G. F. 2009a, Instrument Science Report WFC3-2009-37 (Baltimore, MD: STScI)
Hartig, G. F. 2009b, Instrument Science Report WFC3-2009-38 (Baltimore, MD: STScI)
Hathi, N. P., et al. 2008, AJ, 135, 156
Hathi, N. P., et al. 2010, ApJ, 720, 1708
Hill, D. T., Driver, S. P., Cameron, E., Cross, N. J. G., Liske, J., & Robotham, A. 2010, MNRAS, 404, 1215
Hill, D. T., et al. 2011, MNRAS, in press
Hopkins, A. M. 2004, ApJ, 615, 209
Hopkins, A. M., & Beacom, J. F. 2006, ApJ, 651, 142
Hopkins, P. F., Hernquist, L., Cox, T. J., Di Matteo, T., Robertson, B., & Springel, V. 2006, ApJS, 163, 1
Hopkins, P. F., et al. 2010, ApJ, 715, 202
Kalirai, J. S., et al. 2009a, Instrument Science Report WFC3 2009-31 (Baltimore, MD: STScI)
Kalirai, J. S., et al. 2009b, Instrument Science Report WFC3 2009-30 (Baltimore, MD: STScI)
Kellermann, K. I., Fomalont, E. B., Mainieri, V., Padovani, P., Rosati, P., Shaver, P., Tozzi, P., & Miller, N. 2008, ApJS, 179, 71
Khochfar, S., Silk, J., Windhorst, R. A., & Ryan, R., Jr. 2007, ApJ, 668, L115
Kimble, R. A., MacKenty, J. W., O'Connell, R. W., & Townsend, J. A. the WFC3 Team 2010, BAAS, 215, 46.312
Kinman, T. D., Cacciari, C., Bragaglia, A., Buzzoni, A., & Spagna, A. 2007, MNRAS, 375, 1381
Kitzbichler, M. G., & White, S. D. M. 2007, MNRAS, 376, 2
Klypin, A., Zhao, H., & Somerville, R. S. 2002, ApJ, 573, 597
Koekemoer, A. M., Fruchter, A. S., Hook, R. N., & Hack, W. 2002, in The HST Calibration Workshop: Hubble after the Installation of the ACS and the NICMOS Cooling System, ed. S. Arribas, A. Koekemoer, & B. Whitmore (Baltimore, MD: STScI), 337
Komatsu, E., et al. 2011, ApJS, 192, 18
Kron, R. G. 1980, ApJS, 43, 305
Labbé, I., et al. 2010, ApJ, 716, L103
Law, D. R., et al. 2007, ApJ, 656, 1
Law, D. R., et al. 2009, ApJ, 697, 2057
Lilly, S. J., et al. 1998, ApJ, 500, 75
Luo, B., et al. 2010, ApJS, 187, 560
Luo, B., et al. 2011, ApJS, in press
Lutz, D., et al. 2011, A&A, in press
Madau, P., Pozzetti, L., & Dickinson, M. 1998, ApJ, 498, 106
Majewski, S. R. 1992, ApJS, 78, 87
Malhotra, S., et al. 2005, ApJ, 626, 666
Maybhate, A., et al. 2010, ACS Instrument Handbook, Version 9.0 (Baltimore, MD: STScI)
Melbourne, J., et al. 2005, ApJ, 625, L27
Metcalfe, N., Shanks, T., Campos, A., McCracken, H. J., & Fong, R. 2001, MNRAS, 323, 795
Monaco, P., Fontanot, F., & Taffoni, G. 2007, MNRAS, 375, 1189
Nagamine, K. 2006, ApJ, 653, 881
Nagamine, K., Cen, R., & Hernquist, L. 2005a, ApJ, 618, 23
Nagamine, K., Cen, R., Hernquist, L., Ostriker, J. P., & Springel, V. 2005b, ApJ, 627, 608
Nonino, M., et al. 2009, ApJS, 183, 244
Oesch, P. A., et al. 2010a, ApJ, 709, L16
Oesch, P. A., et al. 2010b, ApJ, 725, L150
Oke, J. B. 1974, ApJS, 27, 21
Papovich, C., Dickinson, M., Giavalisco, M., Conselice, C. J., & Ferguson, H. C. 2005, ApJ, 631, 101
Peng, Y., et al. 2010, ApJ, 721, 193
Petrosian, V. 1976, ApJ, 209, L1
Pickles, A. J. 1998, PASP, 110, 863
Pirzkal, N., et al. 2004, ApJS, 154, 501
Pirzkal, N., et al. 2005, ApJ, 622, 319
Pirzkal, N., et al. 2009, ApJ, 695, 1591
Popesso, P., et al. 2009, A&A, 494, 443
Retzlaff, J., Rosati, P., Dickinson, M., Vandame, B., Rité, C., Nonino, M., Cesarsky, C., & The GOODS Team 2010, A&A, 511, 50
Rhoads, J. E., et al. 2009, ApJ, 697, 942
Robertson, B. E. 2010, ApJ, 713, 1266
Robotham, A., & Driver, S. P. 2011, MNRAS, submitted (arXiv:1101.5187)
Robotham, A., et al. 2010, PASA, 27, 76
Rutkowski, M. J., et al. 2011, ApJ, in press
Ryan, R. E., Jr., Cohen, S. H., Windhorst, R. A., & Silk, J. 2008, ApJ, 678, 751
Ryan, R. E., Jr., Hathi, N. P., Cohen, S. H., & Windhorst, R. A. 2005, ApJ, 631, L159
Ryan, R. E., Jr., et al. 2007, ApJ, 668, 839
Ryan, R. E., Jr., et al. 2011, ApJ, submitted (arXiv:1007.1460)
Scannapieco, E., Silk, J., & Bouwens, R. 2005, ApJ, 635, L13
Somerville, R. S., et al. 2004, ApJ, 600, L171
Steinbring, E., et al. 2004, ApJS, 155, 15
Straughn, A. N., et al. 2008, AJ, 135, 1624
Straughn, A. N., et al. 2009, AJ, 138, 1022
Straughn, A. N., et al. 2011, AJ, 141, 14
van Dokkum, P. G., & Brammer, G. 2010, ApJ, 718, L73
Vanzella, E., et al. 2005, A&A, 434, 53
Vanzella, E., et al. 2009, ApJ, 695, 1163
Windhorst, R. A., Cohen, S. H., Jansen, R. A., Conselice, C., & Yan, H. 2006, New Astron. Rev., 50, 113
Windhorst, R. A., Hathi, N. P., Cohen, S. H., Jansen, R. A., Kawata, D., Driver, S. P., & Gibson, B. 2008, Adv. Space Res., 41, 1965
Windhorst, R. A., Kron, R. G., & Koo, D. C. 1984a, A&AS, 58, 39

Windhorst, R. A., van Heerde, G. M., & Katgert, P. 1984b, A&AS, 58, 1
Windhorst, R. A., et al. 1991, ApJ, 380, 362
Windhorst, R. A., et al. 2002, ApJS, 143, 113
Wong, M. H., Pavlosky, C., & Long, K. S. (ed.) 2010, Wide Field Camera 3 Instrument Handbook, Version 2.0 (Baltimore, MD: STScI)
Wyithe, J. S. B., Yan, H., Windhorst, R. A., & Mao, S. 2011, Nature, 469, 181
Xu, K., et al. 2005, ApJ, 619, L11
Yan, H., Dickinson, M., Eisenhardt, P. R. M., Ferguson, H. C., & Grogin, N. A. 2004, ApJ, 616, 63
Yan, H., & Windhorst, R. A. 2004, ApJ, 612, L93
Yan, H., Windhorst, R. A., Hathi, N. P., Cohen, S. H., Ryan, R. E., O'Connell, R. W., & McCarthy, P. J. 2010, Res. Astron. Astrophys., 10, 867
Yan, H., et al. 2005, ApJ, 634, 109
Yan, H., et al. 2011a, ApJ, 728, L22
Yan, H., et al. 2011b, ApJ, submitted